

Diurnal Variations of the Land–Sea Breeze and Its Related Precipitation over South China

XINGCHAO CHEN

Key Laboratory for Mesoscale Severe Weather, Ministry of Education, and School of Atmospheric Science, Nanjing University, Nanjing, China, and Department of Meteorology, and Center for Advanced Data Assimilation and Predictability Techniques, The Pennsylvania State University, University Park, Pennsylvania

FUQING ZHANG

Department of Meteorology, and Center for Advanced Data Assimilation and Predictability Techniques, The Pennsylvania State University, University Park, Pennsylvania

KUN ZHAO

Key Laboratory for Mesoscale Severe Weather, Ministry of Education, and School of Atmospheric Science, Nanjing University, Nanjing, China

(Manuscript received 5 April 2016, in final form 29 June 2016)

ABSTRACT

Convection-permitting numerical experiments using the Weather Research and Forecasting (WRF) Model are performed to examine the diurnal cycles of land and sea breeze and its related precipitation over the south China coastal region during the mei-yu season. The focus of the analyses is a 10-day simulation initialized with the average of the 0000 UTC gridded global analyses during the 2007–09 mei-yu seasons (11 May–24 June) with diurnally varying cyclic lateral boundary conditions. Despite differences in the rainfall intensity and locations, the simulation verified well against averages of 3-yr ground-based radar, surface, and CMORPH observations and successfully simulated the diurnal variation and propagation of rainfall associated with the land and sea breeze over the south China coastal region. The nocturnal offshore rainfall in this region is found to be induced by the convergence line between the prevailing low-level monsoonal wind and the land breeze. Inhomogeneity of rainfall intensity can be found along the coastline, with heavier rainfall occurring in the region with coastal orography. In the night, the mountain–plain solenoid produced by the coastal terrain can combine with the land breeze to enhance offshore convergence. In the daytime, rainfall propagates inland with the inland penetration of the sea breeze, which can be slowed by the coastal mountains. The cold pool dynamics also plays an essential role in the inland penetration of precipitation and the sea breeze. Dynamic lifting produced by the sea-breeze front is strong enough to produce precipitation, while the intensity of precipitation can be dramatically increased with the latent heating effect.

1. Introduction

The land and sea breeze is a localized circulation driven by the diurnal varying differential heating between land and ocean. This phenomenon can be found in almost every coastal area around the world from the tropics (e.g., Qian 2012) to the polar regions (e.g., Bromwich et al. 2005).

Nowadays, more than 40% of the world population lives within 150 km of the coastline; thus the land- and sea-breeze circulations may have a huge impact on air pollution (e.g., Zhang et al. 2007), precipitation (e.g., Mapes et al. 2003a,b; Warner et al. 2003), and local climate (e.g., Dai et al. 1999) over these regions. The physical mechanisms and dynamical features of the land and sea breeze have been well studied in the literature (e.g., Crosman and Horel 2010; Rotunno 1983). Although the differential heat capacity of land and ocean is the fundamental driving force of land and sea breeze, other geophysical variables like latitude dependence (e.g., Rotunno 1983), ambient wind (e.g., Qian et al. 2009), shoreline curvature (e.g., Baker

Corresponding author address: Professor Kun Zhao, Key Laboratory for Mesoscale Severe Weather, MOE, and School of Atmospheric Science, Nanjing University, 163 Xianlin Avenue, Nanjing 210023, Nanjing, China.
E-mail: zhaokun@nju.edu.cn

et al. 2001), inland terrain (e.g., Qian 2012), atmospheric stability (e.g., Walsh 1974), land cover (e.g., Zhang et al. 2005), land use (e.g., G. Chen et al. 2015), and the urban heat island circulation (e.g., Freitas et al. 2007) can also dramatically influence the characteristics of the land and sea breeze. In consequence, the land- and sea-breeze circulations often vary markedly from region to region.

Diurnal variation of coastal rainfall produced by the land and sea breeze has also been the subject of many past studies (e.g., Burpee and Lahiffi 1984; T.-C. Chen et al. 2014; Zhang et al. 2005), given its significance on coastal weather and climate as well as on human activities. Thermal circulations related to the land and sea breeze can collapse into fronts with potent updrafts along and ahead of the front surfaces (Fovell 2005). When these fronts are lifted by inland terrains (Wang and Kirshbaum 2015) or collide with other boundary layer convergence lines, such as gust fronts (Kingsmill 1995), they can produce intense precipitation and bring extreme meteorological disasters to coastal areas. Meanwhile, latent heating/cooling from precipitating clouds can feed back to the progression and characteristics of the land and sea breeze (e.g., Segal et al. 1986). The land and sea breeze may also induce rainfall far away from the coastline, such as nocturnal offshore convection produced by the convergence line between the land breeze and prevailing onshore wind (Houze et al. 1981; Yu and Jou 2005) and gravity waves (Mapes et al. 2003a).

Several field campaigns were designed to better understanding of coastal rainfall produced by land- and sea-breeze circulations, such as the BMRC Australian Monsoon Experiment (AMEX; Holland et al. 1986), the Land/Sea Breeze Experiment (LASBEX; Banta et al. 1993), the Convection and Precipitation/Electrification Experiment (CaPE; Atkins et al. 1995), and the Dominica Experiment (DOMEX; Wang and Kirshbaum 2015) based on observations from sounding, aircraft, and Doppler lidar. Complimentary insights also come from extensive statistical and climatological studies. Burpee and Lahiffi (1984) used the 3-yr standard surface, upper-air, precipitation, and satellite data to investigate the area-average rainfall variations on sea-breeze days in south Florida. They found that sea breeze can strongly modulate the development of deep convection and produces a sharp midafternoon peak in rainfall. Based on 10 yr of surface rainfall observations, Kousky (1980) found most coastal areas of northeast Brazil have a nocturnal peak in rainfall activity, which is likely attributable to the convergence between the mean onshore flow and offshore land breeze. Kishtawal and Krishnamurti (2001) examined the diurnal cycle of summer rainfall over Taiwan using long-term TRMM Microwave Imager (TMI) observations. They pointed out that the increase of convective activity during the

late afternoon over Taiwan may be induced by localized mass convergence caused by the sea breeze.

However, observations alone may not be sufficient to elucidate all thermodynamic and dynamic processes of the land and sea breeze related to recurring rainfall. Numerical models are often used to simulate and understand the physical mechanisms (e.g., Mapes et al. 2003a). For example, Silva Dias and Machado (1997) used a two-dimensional nonhydrostatic model to compare the development of convection on days with and without the sea breeze in São Paulo, Brazil. Rao and Fuelberg (2000) focused on the role of Kelvin–Helmholtz (KH) instability in determining the time and location of convection behind the sea-breeze front over Cape Canaveral, Florida. Baker et al. (2001) coupled the atmosphere and land surface models to identify the roles of initial soil moisture, coastline curvature, and land-breeze circulations on sea-breeze-initiated precipitation over central Florida. Wapler and Lane (2012) investigated a case of offshore convective initiation by interacting land breezes near Darwin, Australia, using convection-permitting simulations and observation data.

The south China coastal region is one of the maximum rainfall centers in China during the warm season (Luo et al. 2013; Xu et al. 2009). Affected by the coastal terrain, land–sea contrast, and monsoon flow, the diurnal variability of precipitation in the region becomes very complex and is probably produced by various physical processes (e.g., Chen 2009). Through long-term surface (e.g., Yu et al. 2007), satellite (e.g., Chen et al. 2009; Chen 2009), and radar (X. C. Chen et al. 2014, 2015, hereafter C15) observations, diurnal variations of coastal rainfall in the region have been studied extensively in the literature. Results show that the rainfall diurnal variations have profound seasonality (Chen 2009). During late summer (July and August), rainfall occurs mostly in the early afternoon because of the solar heating effect. While, during the mei-yu season (May to June, also called the pre-summer rainy season of south China), rainfall also occurs frequently from midnight to the morning (X. C. Chen et al. 2014). Using 3 yr of radar observations, C15 found that the diurnal cycle of precipitation during the mei-yu seasons is closely related to the land- and sea-breeze circulations. The offshore convergence between the land breeze and prevailing onshore monsoon wind initiates an offshore rainfall line during early night, and this rainfall line is pushed to inland areas by a sea-breeze front during daytime. However, because of the limitations in observations, several key questions remain to be further explored beyond C15, which are the focus of the current modeling study: What are the diurnal variations and vertical structure of the land and sea breeze over this region? What kind of impact does the coastal terrain have on the land and sea breeze and its related rainfall? Will

the related rainfall influence the propagation and intensity of the land and sea breeze as a feedback? In this paper, complementary to the observational study of C15, numerical simulations with the Weather Research and Forecasting (WRF) Model will be employed to answer these questions. Through both control and sensitivity tests, the impacts of coastal mountains, the cold pool dynamics (induced by evaporative cooling of rainfall), and latent heating effects on the land and sea breeze and its related precipitation, diurnal variations will also be investigated. The experimental design is described in section 2. Section 3 presents an overview of the simulations and a comparison with the observations. The impact of coastal terrain on the land and sea breeze and rainfall is discussed in detail in section 4, and the impact of latent heating and cooling effects on the development of daytime rainfall is reported in section 5. Section 6 gives the concluding remarks of the study.

2. Numerical model and experimental design

The Advanced Research WRF Model (Skamarock et al. 2008), version 3.7, is used for this study. Simulations are performed over a single domain that covers most of the south China coastline with 139×199 horizontal grid points and 4-km grid spacing (Fig. 1a). There are 50 vertical levels with the top at 50 hPa and a 5-km sponge layer within the upper part of the model domain. The wind and temperature fields have been relaxed in the sponge layer. An additional experiment raising the top to 10 hPa with an 8-km sponge layer resulted in no apparent difference in simulation results (not shown). In C15, Guangzhou operational radar data were used to investigate the diurnal cycle and propagation of the mei-yu season rainfall over the south China coastal region. The position of the Guangzhou operational radar (GZRD) is shown by a black triangle in Fig. 1a. The black circle (150 km in radius) shows the spatial coverage of the GZRD, which is roughly the Pearl River Delta (PRD) region. The PRD is characterized as a plain surrounded by moderate-height (400–800 m) mountains on the north and the coastline to the south. The model domain is designed to provide a broader coverage of the diurnal variations of land and sea breeze and its related precipitation over the south China coastal region (compared to the coverage of the Guangzhou radar). The model employs the Yonsei University (YSU) boundary layer scheme (Hong et al. 2006), the five-layer thermal diffusion surface model (Skamarock et al. 2008), the Rapid Radiative Transfer Model (RRTM) longwave (Mlawer et al. 1997) and Dudhia shortwave (Dudhia 1989) radiation schemes, and the WRF single-moment 5-class microphysics scheme (Hong et al. 2004).

The primary goal of the experiments is not to simulate each individual event, but to capture the general

characteristics of the diurnal variations of the land and sea breeze and its related rainfall over the south China coastal region during the 2007–09 mei-yu seasons in comparison with the 135-day diurnally averaged radar observations in C15. The initial and lateral boundary conditions are derived from the National Oceanic and Atmospheric Administration (NOAA) Global Forecast System (GFS) $0.5^\circ \times 0.5^\circ$ operational reanalysis data available every 6 h. The control experiment (CNTL) is a 10-day simulation initialized with the 135-day-averaged GFS reanalysis at 0000 UTC and uses the 135-day-averaged GFS reanalysis at 0000, 0600, 1200, and 1800 UTC as boundary conditions, which cycle periodically in time (i.e., from 0000 to 0600 to 1200 to 1800 UTC and then back to 0000 UTC). Similar methodology has also been used to study the diurnal variation of precipitation over other regions (Bao and Zhang 2013; Sun and Zhang 2012; Trier et al. 2010; Zhang et al. 2014). This methodology can filter out temporal variations in environmental conditions across all spatial scales but allow repeated development of diurnal signals such as the land and sea breeze and mountain–plain solenoids (MPS). Unlike in previous research that focused on individual case studies, we averaged three mei-yu seasons of reanalysis data as the initial and boundary conditions.

As shown in Fig. 1a, a large number of bays exist on the south China coast. The biggest one is the Pearl River Bay, located at the center of the domain. These bays can cause the sea breeze to bow landward relative to the straight sections of coastline on either side and induce enhanced upward–downward vertical motion related to the position of bays but distributed asymmetrically (Miller et al. 2003). As a simplification while not losing generality, we used a two-dimensional filter to smooth the coastline in experiment IDEAL (the modified coastline is shown in Fig. 1b). The surface types are also prescribed as water over the ocean and evergreen broadleaf over land to simplify the influence from the underlying surface. Other configurations in IDEAL remain the same as in CNTL. To lessen the sensitivity to model spinup, the first day of the 10-day integrations is excluded for all analyses in this study. Figures 1c and 1d show the mean wind and relative humidity fields at 850 hPa for the final 9 days in CNTL and IDEAL. Low-level wind fields are dominated by southwesterlies in both experiments with higher humidity over the inland area and lower humidity over the ocean area. The mean wind fields on the 0.994-sigma level for the final 9 days in CNTL and IDEAL are shown in Figs. 1e and 1f. Both in CNTL and IDEAL, the near-surface prevailing wind is onshore southerly flow, which transports the warm, moist air from ocean to land.

Three sensitivity experiments (HALF, FAKEDRY, and NOVAP) are designed to further examine the

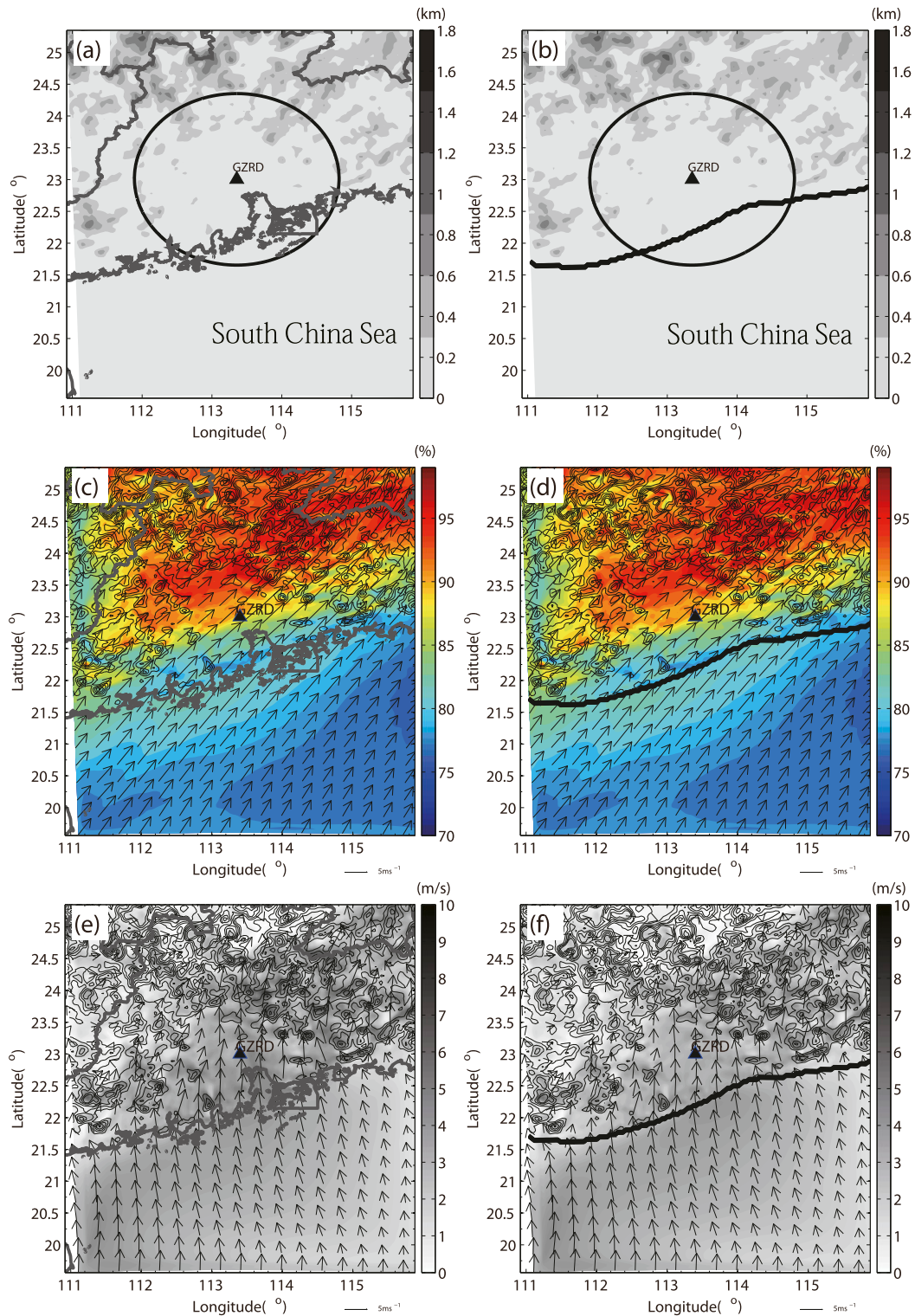


FIG. 1. Model domain and topography with (a) real coastline and provincial borders and (b) modified coastline. Orography is shown by the grayscale. Location of the Guangzhou radar is marked by a black triangle and the 150-km observation range of GZRD is shown with a black circle. The averaged horizontal wind (vectors, m s^{-1} , see reference vector below each panel) and relative humidity (color shadings) at 850 hPa for the final 9 days in (c) the CNTL experiment and (d) the IDEAL experiment. The averaged horizontal wind (vectors, m s^{-1} , see reference vector below each panel) and wind speed (color shadings) at the 0.994-sigma level for the final 9 days in (e) the CNTL experiment and (f) the IDEAL experiment.

TABLE 1. List of control and sensitivity experiments.

Experiment	Coastline	Terrain height	Latent heating and cooling
CNTL	Original	Original	Turned on
IDEAL	Smoothed	Original	Turned on
HALF	Smoothed	Half	Turned on
FAKEDRY	Smoothed	Original	Turned off
NOVAP	Smoothed	Original	Only the cooling associated with the evaporation of liquid water is turned off
HALF-NOVAP	Smoothed	Half	Only the cooling associated with the evaporation of liquid water is turned off

impact of terrain height, cold pool dynamics, and latent heating on the land- and sea-breeze circulations and their related precipitation. All three sensitivity experiments are configured the same as IDEAL, except that terrain height in HALF is reduced to half; all forms of latent heating and cooling (between ice, liquid, and vapor) are turned off in FAKEDRY, and only the cooling associated with the evaporation of liquid water is turned off in NOVAP, which essentially shuts off the mechanisms for cold pool formation from moist convection. The configuration information of different sensitivity experiments is listed in Table 1.

3. Simulation results and comparison with observations

a. Comparison with 3-yr averages of radar and surface observations

The accumulated precipitations of CNTL and IDEAL are compared with the quantitative precipitation estimation (QPE) from GZRD. Figures 2a and 2b present the spatial distributions of GZRD-observed averaged hourly precipitation (averaged hourly precipitation means hourly rainfall normalized by days here) between 0500–0600 and 1500–1600 LST (2100–2200 and 0700–0800 UTC) during the 2007–09 mei-yu seasons. We use Z – R relationships to estimate precipitation intensity (X. C. Chen et al. 2014). Radar echoes are first used to separate convective and stratiform precipitation following Steiner et al. (1995). For convective precipitation, the relationship of $Z = 32.5R^{1.65}$, is used, and, for stratiform precipitation, $Z = 200R^{1.6}$ is applied. The total rainfall refers to the sum of these two types of rainfall. Radar QPE shows an early morning precipitation line along the coastline (Fig. 2a). This line propagates southeast to the open sea in the morning. At noon, another rainfall line is initiated on the inland side of the coastline (not shown here) and then propagates inland in the afternoon (Fig. 2b). At 1500 LST, a new precipitation region can be found on the south slope of mountains in front of this inland-propagating rainfall line (see the dashed circled area in Fig. 2b). In C15, they hypothesized that the

nocturnal offshore rainfall is induced by the land breeze, while the daytime inland-propagating rainfall is closely related to the development of the sea breeze.

Figures 2c and 2d show the spatial distributions of average hourly rainfall for the final 9 days in CNTL. The intensity of rainfall in CNTL is noticeably stronger than that in GZRD observations (different color bars are used in Figs. 2a,b vs Figs. 2c,d), especially for the windward slopes of north mountainous area during the early morning (Fig. 2a vs Fig. 2c). Overprediction of rainfall at the windward slopes during the mei-yu season has also been reported in previous studies of Chien et al. (2002) and Yang et al. (2004), likely because of inadequate resolution, deficiency in the model physics, and/or inaccurate representation of atmospheric flow in the mountainous region. On the other hand, CNTL is an idealized experiment that used the averaged reanalysis data as its initial and boundary conditions to study the general characteristics of the rainfall diurnal cycle while the radar-derived hourly rainfall is an average of many individual precipitation processes. In the meantime, radar QPE may also underestimate the rainfall over complex terrain (Wang et al. 2016). Thus, one should not expect the CNTL-simulated rainfall to match exactly what was derived from the radar estimation during these three mei-yu seasons. Nevertheless, despite differences in the rainfall intensity and locations, CNTL still can capture the basic diurnal features of the land-and-sea-breeze-related precipitation with timing and location similar to the observations: that is, the early morning rainfall line along the coastline (Fig. 2c) and the inland-propagating rainfall line during afternoon (Fig. 2d). For the IDEAL case, after the modification of coastline shape and simplification of the underlying surface types, the diurnal variation of precipitation is still very similar with CNTL (Figs. 2e,f).

Wind observations from two national automatic weather stations (AWS, shown by black squares in Fig. 2a) have also been used to further investigate whether the IDEAL experiment can properly simulate the land and sea breeze over south China. Figure 3 shows the diurnal variations of the perturbation wind

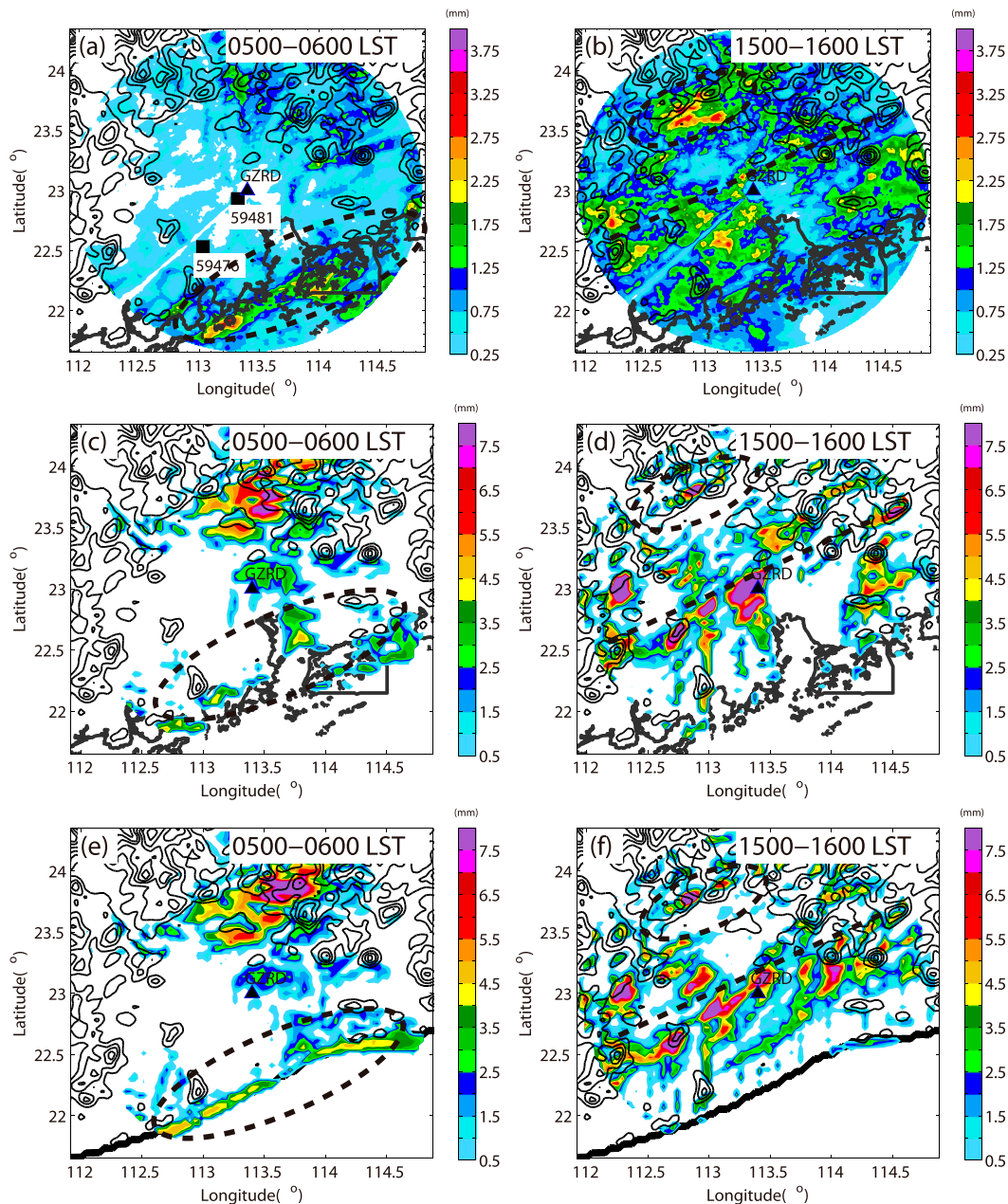


FIG. 2. Spatial distributions of average hourly precipitation (mm) between (left) 0500–0600 and (right) 1500–1600 LST from (a),(b) GZRD QPE; (c),(d) the CNTL experiment; and (e),(f) the IDEAL experiment. The black squares in (a) show the spatial distributions of two AWS stations (IDs: 59476 and 59481). Orography is superimposed onto each panel and is shown as black contours with a 150-m interval. The heavy solid lines in (e) and (f) indicate the modified coastlines, and the dashed lines in (b), (d), and (f) indicate the precipitation lines. The heavy black dashed circles in the left and right columns indicate the precipitation lines along the coastline and inland mountainous area, respectively.

(subtract the average daily mean wind) direction and speed at the 10-m height observed by these two stations during the 2007–09 mei-yu seasons (shown by black lines). Perturbation wind with a direction between 90° and 270° is offshore (land breeze), and that with a direction smaller than 90° or larger than 270° is onshore

(sea breeze). Over the coastal regions, the sea breeze begins to establish around noon and turns to a land breeze near midnight (Figs. 3a,b). Diurnal cycles of the simulated perturbation wind direction at the 10-m height over these two stations in IDEAL are shown by the red lines in Figs. 3a and 3b. It is found that IDEAL

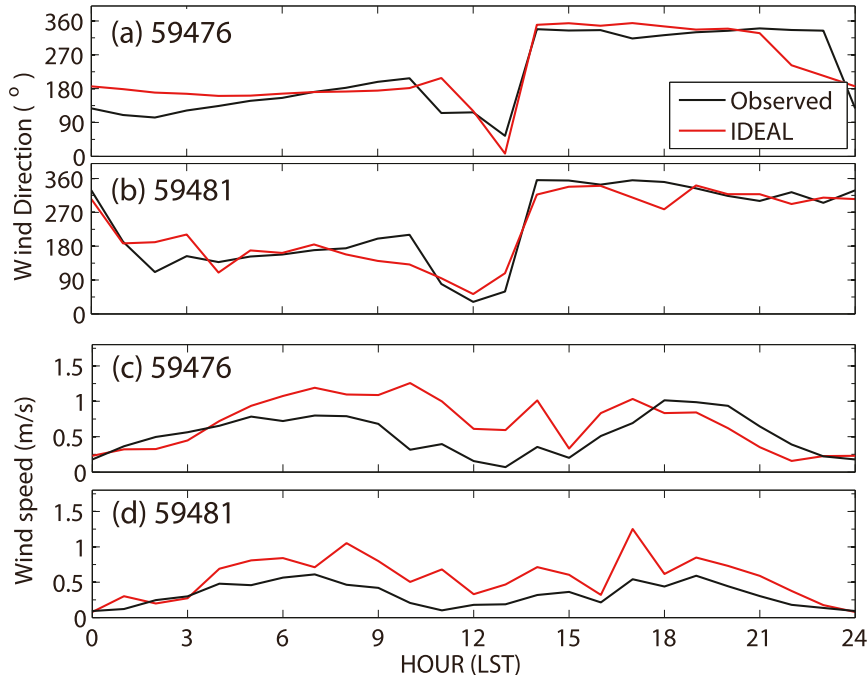


FIG. 3. Diurnal variations of perturbation wind (a),(b) direction and (c),(d) speed at 10-m height observed by AWS (a),(c) 59476 and (b),(d) 59481 (black lines). Simulated diurnal variations of perturbation wind direction and speed at 10-m height near the two AWS stations in the IDEAL experiment are shown in red lines.

verified well against the AWS observations (Figs. 3a,b). The diurnal cycles of the observed and simulated perturbation wind speed at the 10-m height over these two stations also have a similar pattern (Figs. 3c,d), except that the simulated wind speed is slightly larger. Overall, the diurnal variations of the land and sea breeze can be captured over both stations in IDEAL. Also, the diurnal variations of the land and sea breeze can be affected by the combined forcing of both the diurnal and semidiurnal modes. Using the Fourier analysis method, we have compared the diurnal and semidiurnal modes of the surface perturbation wind directions in observations and IDEAL. The results show that both modes can be captured in IDEAL (not shown here). This level of agreement means that we can examine the mechanisms of the land and sea breeze and its related rainfall with the simpler coastline configuration. All analysis hereinafter will focus on the simulation results of IDEAL unless otherwise specified.

b. Overview of simulated rainfall in IDEAL

Figure 4 shows the spatial distribution of average hourly rainfall in IDEAL over the whole model domain (Fig. 1b). Similar to C15, the diurnal variation of rainfall over the south China coastal region can be divided into two stages: from night to early morning, rainfall is initiated along the coastline (Figs. 4a,b) and forms into an offshore rainfall line parallel to the coastline (Figs. 4c,d).

By noontime, the original precipitation line propagates to the offshore direction, and a new rainfall line begins to form inland, highlighted by the dashed line in Fig. 4e. From early to late afternoon, this rainfall line propagates to inland areas with a new rainfall zone forming on the south slope of the inland mountains (Figs. 4f,g). This line finally dissipates in the evening (Fig. 4h).

There is strong inhomogeneity of rainfall intensity along the coastline with heavier rainfall occurring in the regions with coastal mountains during the initiation stage of the nocturnal offshore rainfall line (Figs. 4a,b, highlighted by black dashed circles). Because the heavier rainfall regions are out of the coverage area of GZRD, the high-resolution global precipitation dataset from NOAA's Climate Prediction Center Morphing Technique (CMORPH; Joyce et al. 2004) during the 2007–09 mei-yu seasons is used to verify the simulation results. CMORPH has been verified with Chinese rain gauge reports from ~ 2000 stations and exhibits the best performance among satellite precipitation estimates in depicting the spatial pattern and temporal variations (available every 30 min and every $0.007^\circ \times 0.007^\circ$ in latitude–longitude) of precipitation (Shen et al. 2010). Figure 5 shows the spatial distribution of average hourly rainfall over the simulation domain between 0000 and 0100 LST. Similar to the simulations in IDEAL, CMORPH shows two nocturnal rainfall maxima near the

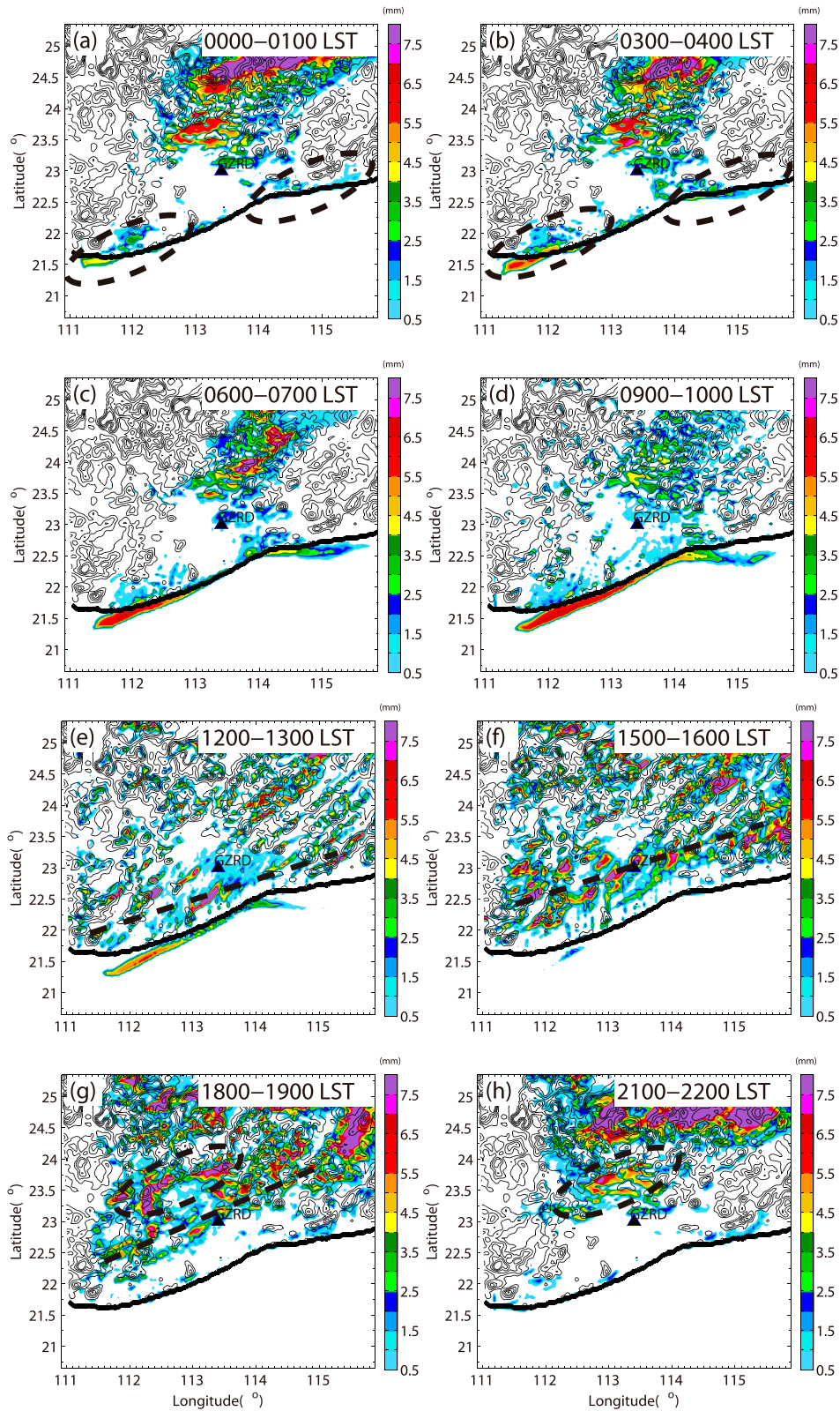


FIG. 4. Spatial distributions of average hourly precipitation (mm) between (a) 0000 and 0100; (b) 0300 and 0400; (c) 0600 and 0700; (d) 0900 and 1000; (e) 1200 and 1300; (f) 1500 and 1600; (g) 1800 and 1900; and (h) 2100 and 2200 LST in the IDEAL experiment. Orography is superimposed onto each panel and is shown as black contours with a 150-m interval. The heavy solid lines indicate the coastlines, and the dashed lines indicate the precipitation lines. The heavy black dashed circles indicate the rainfall maxima.

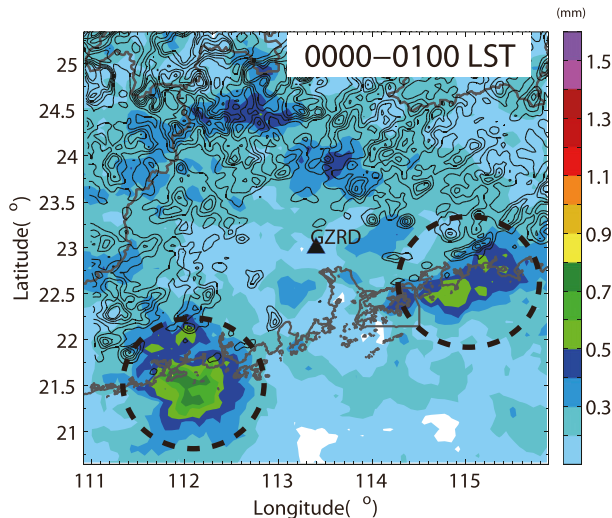


FIG. 5. Spatial distributions of average hourly precipitation between 0000 and 0100 LST in CMORPH observations. Orography is superimposed onto each panel and is shown as black contours with a 150-m interval. Two nocturnal rainfall maxima near the mountainous region along the coastline are indicated by the heavy black dashed circles.

mountainous region along the coast. In contrast, precipitation is much weaker over the flat coastal regions (in the middle of two coastal rainfall maxima). This inhomogeneity shows that the coastal terrain can distinctly influence the diurnal variation of the land and sea breeze, which can further change the strength of its related precipitation. The detailed impacts of the coastal terrain height on nocturnal offshore precipitation will be discussed in the next section.

4. Diurnal variations of the land and sea breeze and the impact of coastal terrain

In this section, the development and evolutions of the land and sea breeze in the south China coastal regions will be documented, with a focus on the differences between the regions with and without coastal orography. A sensitivity experiment on terrain height (HALF) is designed to examine the possible physical mechanisms of the inhomogeneity of nocturnal coastal rainfall.

a. Diurnal cycle of the land and sea breeze

Figure 6 shows the hourly evolution of the land breeze over the south China coastal region from 0100 to 0800 LST. The average daily mean wind has been subtracted to reveal more clearly the diurnal variations of coastal circulations. The perturbation north–south wind component v' is further colored to represent the strength of the land and sea breeze, since the coastline is oriented approximately in the east–west direction. Hours after the sunset (Fig. 6a), there still exists a weak residual sea breeze over the inland area. At the same time, a clear

but weak land breeze begins to establish along the coastline. The land breeze becomes stronger and extends to farther onshore and offshore regions from 0200 to 0700 LST (Figs. 6b–g). Over the subregions with coastal mountains, the land breeze and the convergence ahead (not shown here) are much stronger than other subregions, which leads to stronger updraft and heavier rainfall over these mountainous regions, as described in section 3. In the early morning, the land breeze reaches its strongest stage (Fig. 6h). Almost all inland and offshore areas over the south China coastal region are featured as offshore perturbation wind except for some inland mountainous areas that are far from the coastline. The strongest offshore perturbation wind is still located around the coastline at this time. As shown in Figs. 4a–d, the nocturnal offshore rainfall line from 0100 to 0800 LST is triggered in front of the land breeze, consistent with the observational analysis of C15. This indicates that initiation of offshore rainfall line over this region is closely related to the convergence between the land breeze and the prevailing low-level onshore wind (Fig. 1d).

Development of sea breeze over the south China coastal region is shown in Fig. 7. At noontime, the residual land breeze can still be found over some inland plain regions. For the inland mountainous regions, the flow has already changed to the onshore direction. This is closely related to the MPS circulation and will be discussed later. At the same time, sea breeze begins to establish along the coastline (Fig. 7a), though it is rather weak, given that the surface temperature contrast is still small between inland and ocean surface at this time (not shown). An inland rainfall line can be found along the front of the sea breeze, where convergence between the sea breeze and the residual offshore wind can be found (Fig. 4e). With an increase in solar heating, wind speed of the sea breeze becomes stronger. The sea breeze extends farther inland and to the offshore regions during the early afternoon (Figs. 7b–d). The rainfall line also propagates to the inland areas associated with the inland penetration of the sea-breeze front (Fig. 4f). The line of maximum onshore wind stays around the coastline with little inland propagation but becomes wider in the direction normal to the coastline during these 3 h. In the late afternoon, the line of maximum onshore wind quickly propagates to the inland areas (Figs. 7e–g). Meanwhile, a gust front is formed ahead of the rainfall line, and, subsequently, a new precipitation zone forms on the south slope of the inland mountains (Fig. 4g). There are clear along-coast variations in inland penetrating speed of the sea breeze. The inland-propagation speed of the sea-breeze front is faster over the plain areas (in the center on the line) and slower over

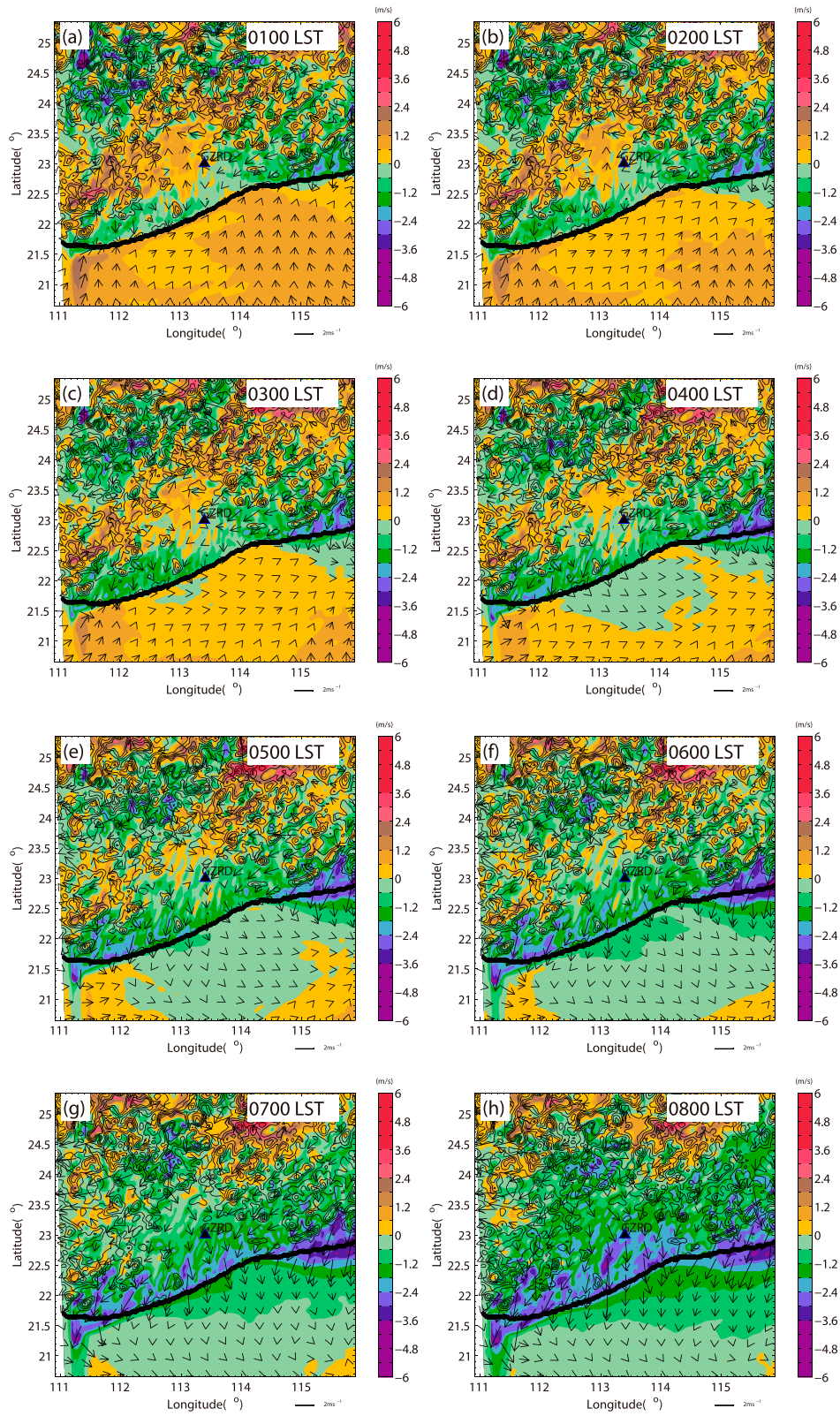


FIG. 6. Perturbation wind (vectors, m s^{-1} , see reference vector below each panel) and v' (color-filled contours) on the 0.994-sigma level at (a) 0100, (b) 0200, (c) 0300, (d) 0400, (e) 0500, (f) 0600, (g) 0700, and (h) 0800 LST. Orography is superimposed onto each panel and is shown as black contours with a 150-m interval. The heavy black solid lines indicate the coastlines.

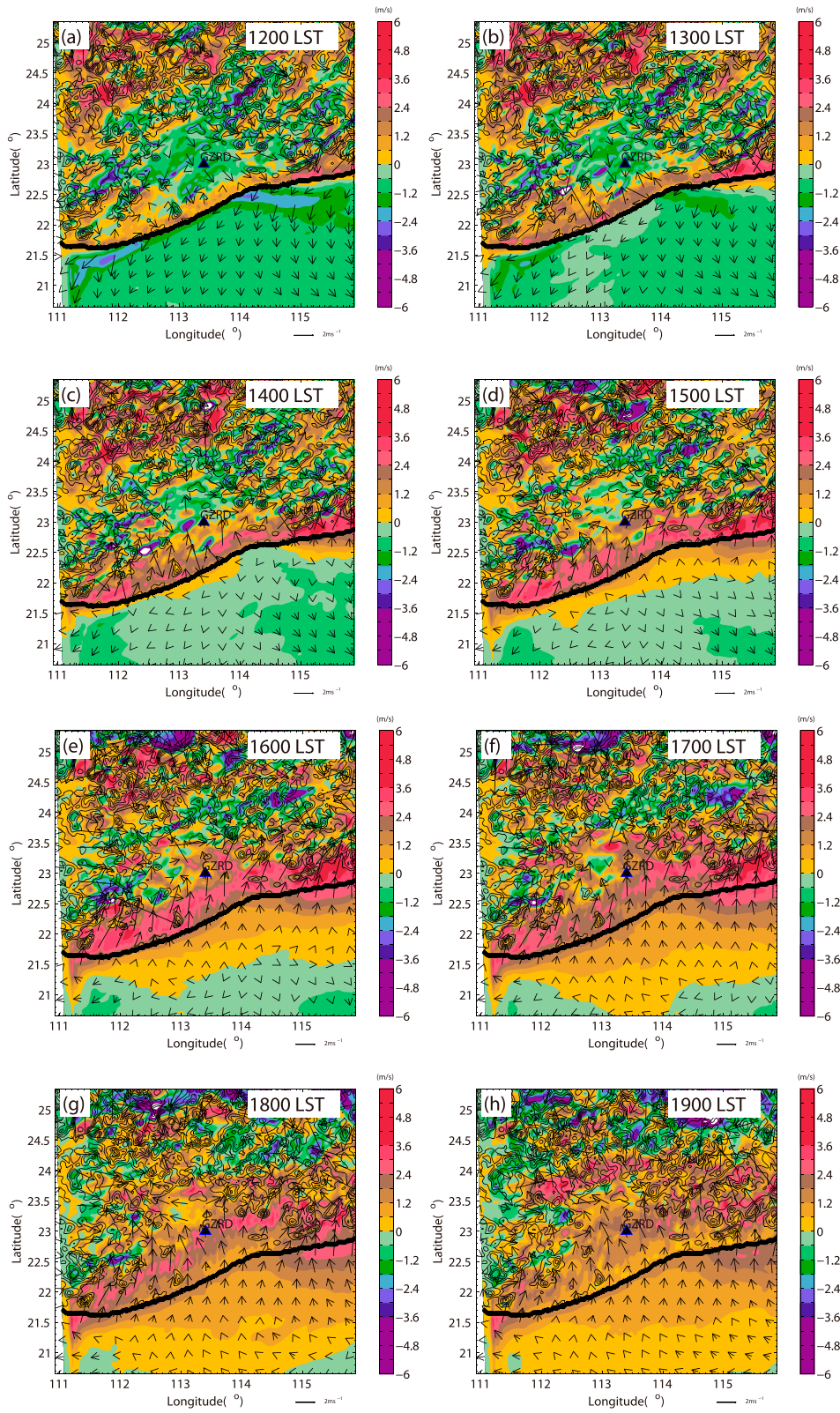


FIG. 7. As in Fig. 5, but for (a) 1200, (b) 1300, (c) 1400, (d) 1500, (e) 1600, (f) 1700, (g) 1800, and (h) 1900 LST.

the mountainous areas (on both sides of the line). In the early evening, the sea-breeze circulation reaches its mature stage, while most of the inland areas are covered by onshore wind except for some mountainous regions. The original maximum onshore wind line dissipates, while the new onshore wind maximum on the south slope of inland mountains remains at this time (Fig. 7h).

To elucidate the impact of coastal terrain on the land- and sea-breeze circulation, the cross sections over different subregions with and without coastal terrains are presented in Figs. 8 and 9. Figure 8 shows the diurnal variation of the perturbation wind field over the subregion with coastal mountains (shown by the green box in Fig. 8a). All Hovmöller (Fig. 8b) and cross-sectional (Figs. 8c–j) diagrams have the same horizontal spatial dimension, which is along the meridian of the green box (shown by the red arrow) and zonally averaged (Fig. 8a). The Hovmöller diagram of v' on the second lowest model level (the 0.994-sigma level, about 50 m above the surface) is shown in Fig. 8b. Consistent with the daily evolutions of the surface wind in Figs. 6 and 7, clear land- and sea-breeze circulations can be found. Over the subregion, the land breeze begins to establish on the coastline (around 21.5°N) from 0000 LST. The strength of the land breeze increases gradually and reaches its strongest stage around 0800 LST. Accompanied by the strengthening process, expansion of the land breeze can also be found both onshore and offshore. The offshore part of the land breeze over this region is very robust, which induces a strong convergence in its leading edge (Fig. 8b). The offshore convergence becomes the strongest around 0500 LST and falls off then. Wind on the coastline changes to an onshore sea breeze from 1200 LST. The sea breeze reaches its strongest stage on the coastline at 1500 LST and begins to expand farther both onshore and offshore. The inland-propagation speed of the sea breeze is rather small over this subregion (around 2.3 m s^{-1} on average, estimated from Fig. 8b). Especially from 1500 to 2000 LST, the sea breeze almost stalls at the coastline with little inland propagation (see also Fig. 7b). Besides the diurnal variation of the land- and sea-breeze circulations, an MPS circulation can also be clearly found around 24°N between the inland mountain and basin. The cross section of the north–south mean wind component v (color-filled contours), equivalent potential temperature (black contours), and mean wind vectors (arrows) is shown in Fig. 8c. We can find that the averaged prevailing low-level wind is onshore wind, which brings warm, moist air from ocean to land. However, the speed of this onshore wind has an obvious decrease around the coastline because of the blockage of coastal mountains.

To further reveal the diurnal variations of the land and sea circulation over this subregion, Figs. 8d–j show the cross sections of (at 4-h intervals) the north–south perturbation wind component v' (color-filled contours), the equivalent potential temperature (black contours), and perturbation wind vectors (arrows) over this subregion. At 0000 LST, most coastal areas from 21° to 23°N are still featured as a sea breeze (Fig. 8d). Only the wind on the lowest 100-m levels near the coastline has changed to a land breeze (Fig. 8b). At 0400 LST, the thickness of the land breeze over the coast region increases, and the wind speed also becomes stronger (Fig. 8e). Negative v' can be found above the basin, which is the downslope wind of the nighttime MPS circulation. In the early morning, the land breeze reaches its strongest stage (Fig. 8f). At this time, a clear circulation (shown by the red cycle in Fig. 8f, combination of the land breeze and the downslope wind of coastal mountains) can be found between the coastal mountains and the open ocean, with the updraft over the ocean and downdraft over the coastal mountains. At noontime (1200 LST; Fig. 8g), with the increase of solar heating, convection can be clearly found over the inland area and the temperature gradient between coastal mountains and the ocean is much stronger than that in the early morning (Fig. 8f). Surface solar heating over the mountain ranges and the adjacent slopes has driven a flow reversal from the nighttime pattern. A clear up-slope flow can be found on the coastal slope of inland mountains (around 24°N). Sea breeze also begins to establish along the coastline (Fig. 8b) but still under the lowest 200 m and much weaker than the inland MPS circulation. At 1600 LST (Fig. 8h), convection over inland regions becomes rather vigorous, and the temperature gradient between the coastal mountains and ocean reaches its strongest stage. Both the sea breeze and MPS circulations between the inland basin and the mountains are very clear at this time, with an offshore direction compensating flow above the low-level onshore winds. The inland penetration of the sea breeze is blocked by the coastal mountains and mainly stalls over the south side of the mountain peak. During the evening hours (2000 LST; Fig. 8i), the sea breeze has merged with the downslope wind of the MPS circulation around 22.3°N, and most inland areas feature an onshore wind. Downslope winds have also become established on the slope of inland mountains (around 24°N) at this time.

Figure 9 shows diurnal variations of the perturbation wind field over the subregion without coastal mountains (shown by the red box in Fig. 9a). As in Fig. 8b, a clear land- and sea-breeze circulation can be found on the Hovmöller diagram in Fig. 9b. Both the land and sea breeze begin to develop along the coastline (around

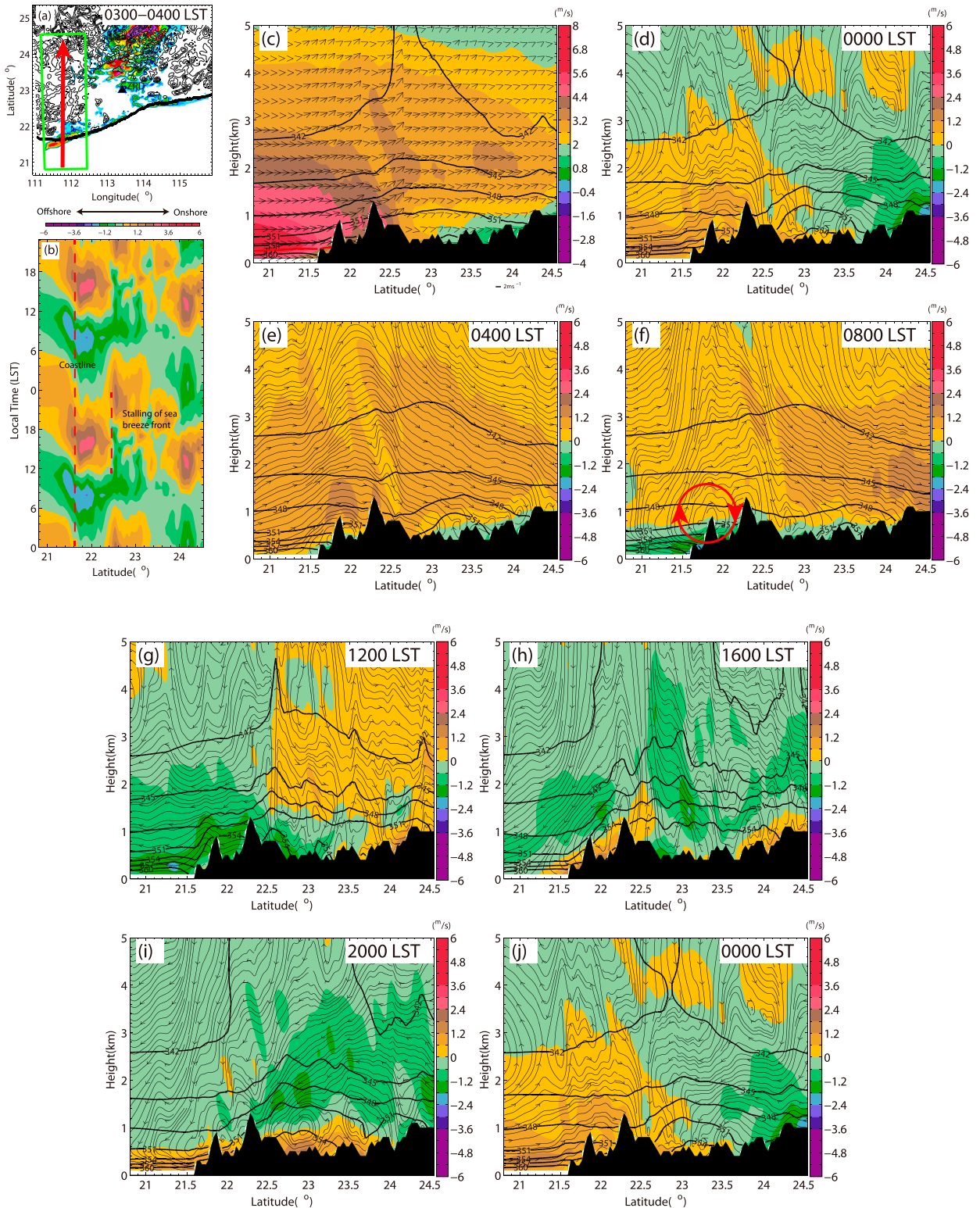


FIG. 8. (a) Averaged hourly precipitation (mm) between 0300 and 0400 LST. Orography is superimposed onto each panel and is shown as black contours with a 150-m interval. (b) Hovmöller diagram of zonal-averaged perturbation v' (m s^{-1}) at the 0.994-sigma level along the meridian of the green box in Fig. 8a. (c) Cross section of mean wind vectors (v and w), v (color-filled contours), and equivalent potential temperature (black contours, K). Cross sections of perturbation wind vector (v' and w' , streamlines) and v' (color-filled contours) and equivalent potential temperature (black contours, K) at (d) 0000, (e) 0400, (f) 0800, (g) 1200, (h) 1600, (i) 2000, and (j) 0000 LST. All cross sections are zonal averaged along the meridian of the green box in Fig. 8a. The interpolated topographic profiles are shown by the black shading.

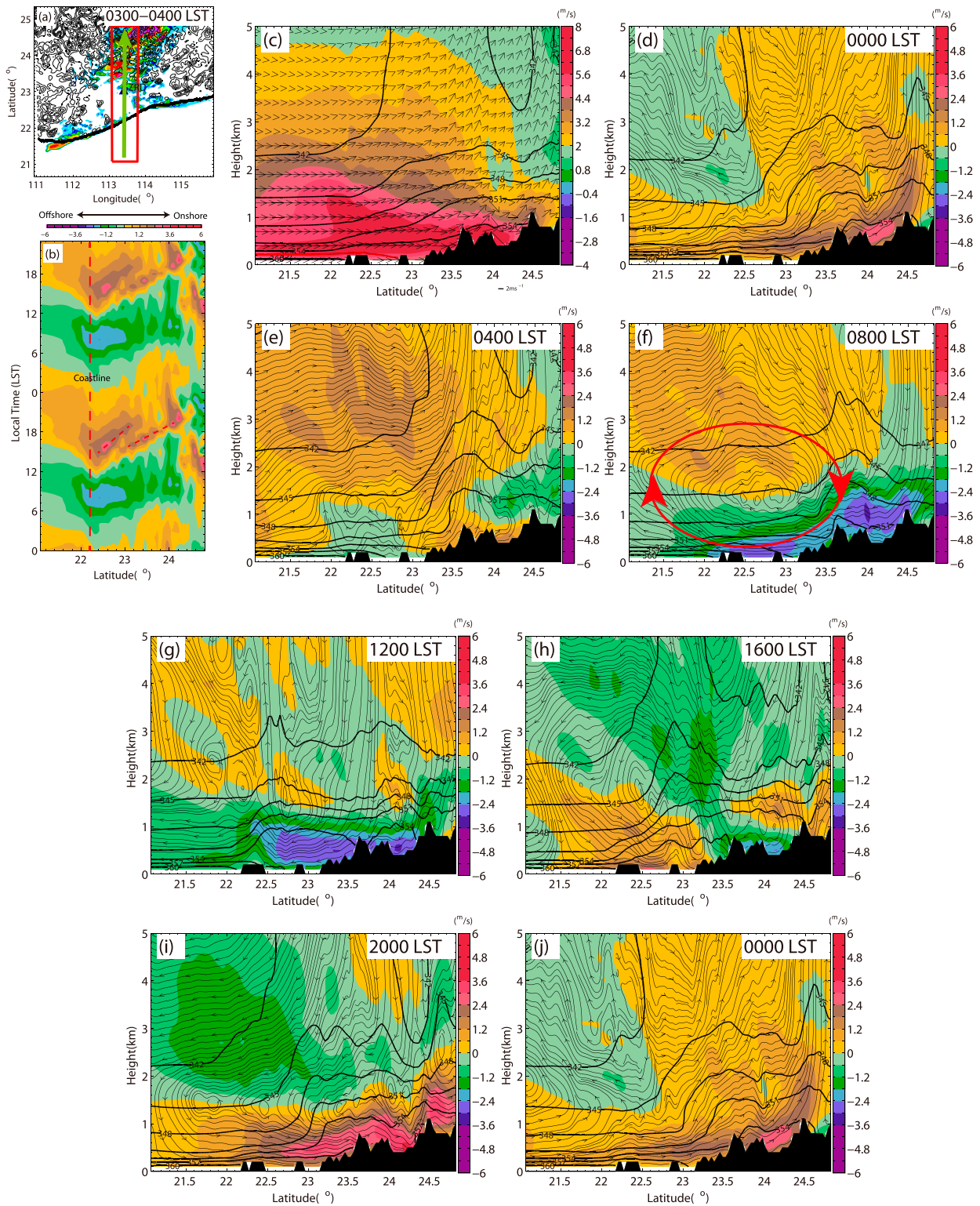


FIG. 9. As in Fig. 8, but for the red box highlighted in Fig. 9a.

22.2°N) and then expand farther inland and offshore, which is consistent with the mountainous subregion as shown in Fig. 8b. However, obvious differences can also be found for both the land-breeze and sea-breeze circulations between these two subregions. For the land breeze, the initiation over this flat subregion is about 1.5 h later than that over the mountainous subregion. Also, the intensity of the land breeze and the offshore convergence in front of the land breeze over the ocean surface is weaker, which can explain why nocturnal precipitation along the coastline in this subregion is weaker than that over the mountainous subregion, with detailed physical mechanisms discussed later. For the sea breeze, the initiation over the flat subregion is 1 h later than that over the mountainous subregion. After the sea breeze reaches its strongest stage around 1500 LST, its leading front propagates farther inland with an inland-propagating speed around 3.5 m s^{-1} , while there is another offshore expansion of the sea breeze with the leading-edge-propagating speed around 3.3 m s^{-1} . The faster inland propagation of sea breeze may be related to the absence of the coastal mountains in this subregion. In the meantime, another convergence line initiated around 1500 LST can be found farther inland ($\sim 25 \text{ km}$) north of the sea breeze (Figs. 9b, 7e), which subsequently induces new precipitation on the south slope of the inland mountains (see also Fig. 4). This new convergence line is likely a gust front produced by the cold pool to be further discussed in section 5. As in Fig. 8c, the prevailing low-level wind along this cross section is directed onshore. Without the blockage of coastal mountains, this onshore wind can bring moist, warm air from ocean to an area farther inland (Fig. 9c).

At 0000 LST (Fig. 9d), most areas over this region are still dominated by a sea breeze (onshore perturbation wind). By 0400 LST (Fig. 9e), a clear land breeze can be found near the coastline, which reaches its mature stage at 0800 LST (Fig. 9f). The circulation (shown by the red cycle in Fig. 9f, a combination of the land breeze and the downslope wind of inland mountains) between the ocean and inland areas over this subregion is much broader, with weaker updraft over the ocean surface (Fig. 9f) than that over the subregion with coastal mountains (Fig. 8f). In the meantime, there is a nighttime MPS circulation developed between the inland mountains and plain around 24°N at 0800 LST that is distinct from the land- and sea-breeze circulations over the ocean (Fig. 9f). At noon (1200 LST; Fig. 9g), with the increased solar heating, the horizontal temperature gradient between coastal mountains and the ocean is strengthened; however, there is no clear sea breeze at this time. At 1600 LST (Fig. 9h), convection over inland regions becomes rather vigorous. A sea-breeze circulation between ocean and land is

clearly established, with the offshore-directed compensating wind above the low-level onshore winds. With no coastal mountains, the sea breeze propagates inland more easily, reaching the most inland area by the evening (2000 LST; Fig. 9i) and then subsequently merges with the inland MPS circulation (between the plains and the inland mountains). Meanwhile, the offshore compensating wind remains visible above the low-level onshore wind.

b. Sensitivity experiment on terrain height (HALF)

As described in previous sections, the coastal mountains can be very influential to the intensity of nocturnal offshore rainfall. The impact of the coastal terrain on the nocturnal offshore rainfall has been studied over many different coastal areas by observations (e.g., Yu and Jou 2005) and numerical models (e.g., Barthlott et al. 2014; Mapes et al. 2003a). To further investigate the effect of coastal mountain height on the nocturnal offshore rainfall over south China, experiment HALF is performed, in which all the terrain has been reduced to half of the original height.

Figure 10a shows the difference of the wind fields between IDEAL and HALF (IDEAL minus HALF) along the cross section shown in Fig. 8a. Only the coastal area and the lowest 1 km are shown here. At 0000 LST, around the initiation time of offshore precipitation, an additional circulation can be found above the slope of coastal mountains with a low-level offshore (or down-slope) wind and an onshore (or upslope) compensating wind above it when the terrain is higher (IDEAL). Associated with the low-level offshore wind is stronger low-level convergence that can induce strong offshore precipitation near the coastline during the night (Figs. 10d,e). The characteristics of this circulation are similar to the nighttime MPS in previous studies (e.g., Sun and Zhang 2012; Zhang et al. 2014). Moreover convection initiation, and subsequent precipitation due to the lift of coastal terrains, may produce a cold pool on the windward slope, which can further induce an offshore-directed wind (Qian 2012).

To elucidate the physical mechanisms responsible for the formation of the stronger nocturnal offshore rainfall over this subregion with coastal terrains, we further compared experiments NOVAP and HALF-NOVAP, as shown in Fig. 10b. The only difference between NOVAP (HALF-NOVAP) and IDEAL (HALF) is that cooling associated with evaporation is turned off, which essentially shuts off the mechanisms for cold pool formation from moist convection. Without the cold pool, a stronger circulation can still be found over the seaward slope of the coastal mountains in NOVAP than IDEAL, indicating that the cold pool dynamics may not be essential for the nocturnal downslope wind over the

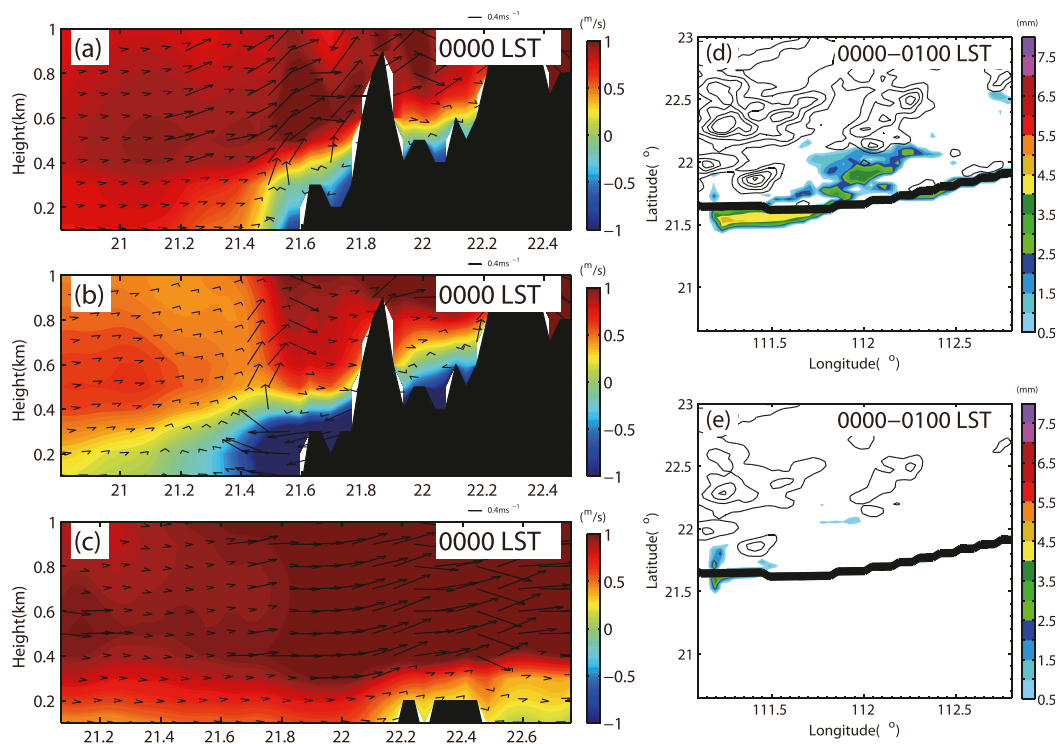


FIG. 10. Differences of v' (color-filled contours, m s^{-1}) and wind vectors (m s^{-1} , vector above each panel = 0.4 m s^{-1}): (a) between IDEAL and HALF experiments along the cross section shown by the green box in Fig. 8a, (b) between NOVAP and HALF-NOVAP experiments along the cross section shown by the green box in Fig. 8a, and (c) between IDEAL and HALF experiments along the cross section shown by the red box in Fig. 9a at 0000 LST. The interpolated topographic profiles are shown by black shading. Spatial distributions of average hourly precipitation between 0000 and 0100 LST in the (d) IDEAL and (e) HALF experiments. Orography is superimposed onto the figure in black contours with a 150-m interval. The heavy black solid line in (d) and (e) indicates the coastline.

coastal mountains. In contrast, Fig. 10c shows the difference in the wind fields between IDEAL and HALF experiments along the cross section shown in Fig. 9a. With mountains much farther away from the coastlines, MPS associated with the inland mountains has less influence over the coastal region along this cross section. Consequently, the offshore wind and convergence have no apparent weakening with the decrease of the inland terrain height (Fig. 10c). Results from these sensitivity experiments suggest that the MPS circulation produced by the coastal terrain can combine with the land breeze that strengthens the offshore convergence during night, which is likely the primary reason why the mountainous coastal region has stronger nocturnal offshore rainfall.

5. Thermodynamics in inland propagations of sea breeze and precipitation

There are two main factors causing the formation of a sea-breeze circulation. The first is differential heating in the boundary layer due to the land and sea contrasts. The second is the latent heating and cooling effect in

precipitating clouds triggered by the boundary layer circulation (Khain et al. 1996). As pointed out by Nicholls et al. (1991) and Boybeyi and Raman (1992), the thermodynamic forcing of convection plays a very important role in the sea-breeze circulation. But among the literature based on linear and analytical models (e.g., Dalu and Pielke 1989; Drobinski and Dubos 2009; Niino 1987; Qian et al. 2009; Rotunno 1983), few studies have focused on the influence of the latent heating and cooling effects of sea breeze and its related precipitation.

To illuminate the impact of the latent heating and cooling effects, only the sea breeze and daytime precipitation over the subregion without coastal mountains will be examined here (the red box in Fig. 9a). Latent heat release from condensation can reinforce the updraft that sustains growing precipitation particles and prevents them from falling out of the clouds earlier, both of which can lead to stronger thunderstorms and heavier rainfall. On the other hand, evaporative cooling from precipitation produces a surface cold pool, which can initiate new convection and accelerate the propagation of updraft and rainfall belt (e.g., Bao and Zhang 2013).

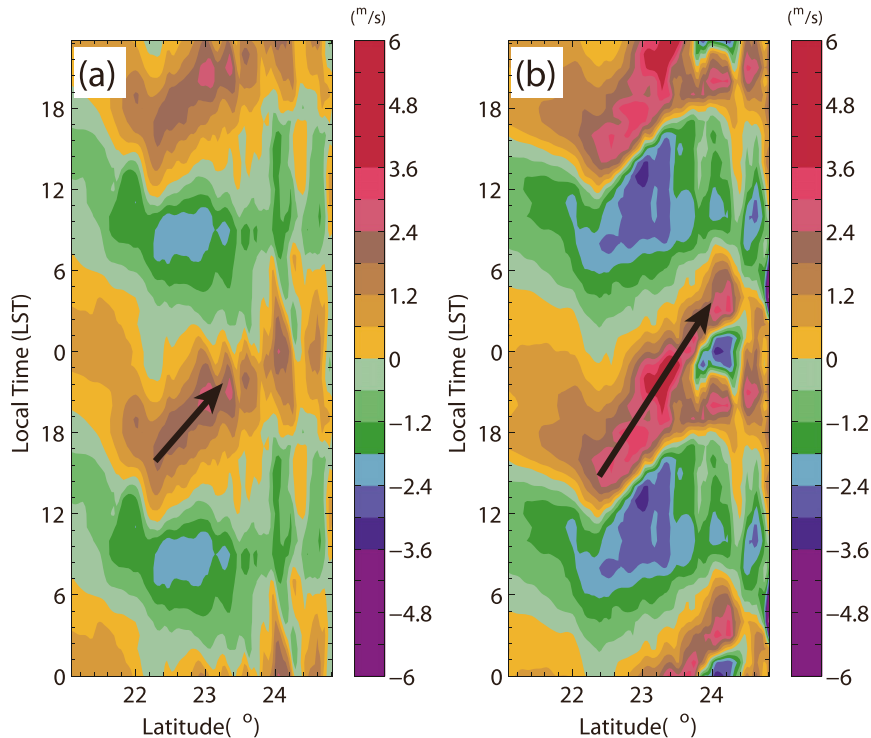


FIG. 11. Hovmöller diagrams of v' (m s^{-1}) at the 0.994-sigma level along the meridian of the red box in Fig. 9a and averaged along the zonal direction of this box in (a) FAKEDRY and (b) NOVAP.

The FAKEDRY and NOVAP experiments are performed to analyze how latent heating and cold pools can influence the development and penetration of sea breeze and the associated precipitation in the subregion without coastal topography.

The Hovmöller diagrams (along the meridional axis in Fig. 9a) of v' on the second lowest model level (the 0.994-sigma level, about 50 m above the surface) of FAKEDRY and NOVAP are shown in Fig. 11. As discussed in section 4a, the sea breeze in IDEAL begins to establish along the coastline from 1200 LST and subsequently propagates inland at a speed of around 3.5 m s^{-1} (Fig. 9b). A gust front produced by the cold pool can be found north of the sea-breeze front. This gust front induces new precipitation on the south slope of inland mountains later (Fig. 4g). For FAKEDRY, the initiation time of sea breeze is also at 1200 LST. The speed of the inland propagation of the sea breeze in FAKEDRY is around 3.0 m s^{-1} (Fig. 11a), which is slightly slower than IDEAL (Fig. 9b). Since all the latent heating and cooling is shut off in FAKEDRY, no gust front can be found in front of the sea breeze. For the NOVAP experiment, the inland-propagating speed (around 1.2 m s^{-1}) of the sea breeze is much slower than in both IDEAL (Fig. 9b) and FAKEDRY

(Fig. 11b). Rainfall is much heavier in NOVAP (not shown here) because the local convection is enhanced in the absence of evaporative cooling (Bao and Zhang 2013). The gust front is also absent in NOVAP because the cold pool formation from moist convection has been essentially shut off.

The difference in inland sea-breeze propagation between the above three experiments implies that convection initiated by the sea breeze can impede the inland propagation of the sea-breeze boundary (Fig. 11a vs Fig. 11b), while the cold pool produced by the convection can increase the inland-propagation speed (Fig. 9b vs Fig. 11b). The convective impediment may be induced by the ambient cloud cover of convection, which could weaken sea breeze because of the loss of incoming solar radiation (Segal et al. 1986). However, the detailed physical mechanisms still need further investigations.

Since the inland-penetrating speeds of sea breezes in IDEAL and FAKEDRY are similar, the associated precipitation from these two experiments is further compared. The hourly rainfall in IDEAL and FAKEDRY is shown in Fig. 12. From 1300 to 1600 LST, distinct rainfall lines can be found in both the IDEAL and FAKEDRY experiments. The intensity of precipitation in FAKEDRY is much weaker than in

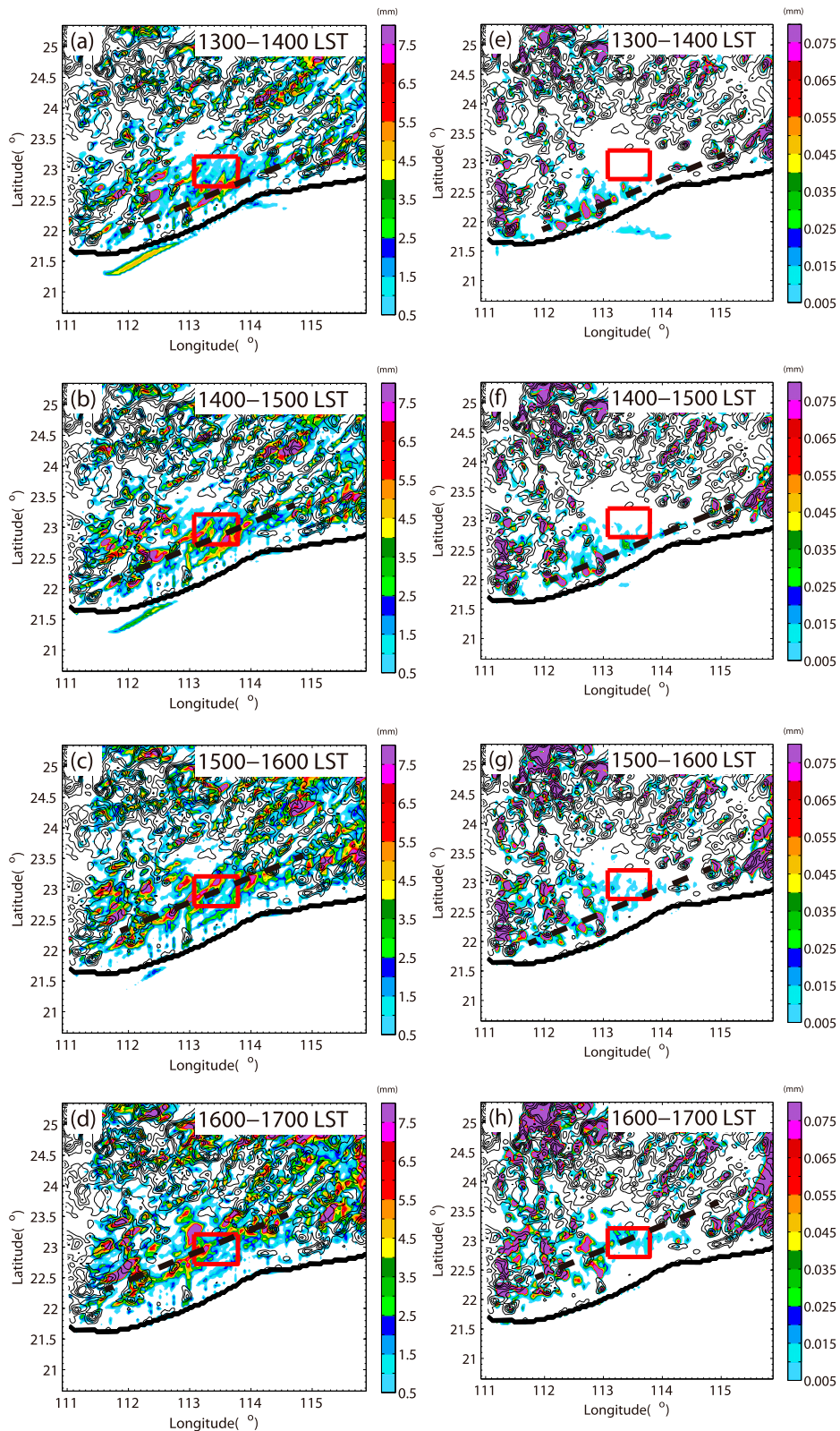


FIG. 12. Spatial distributions of average hourly precipitation between (a),(e) 1300 and 1400; (b),(f) 1400 and 1500; (c),(g) 1500 and 1600; and (d),(h) 1600 and 1700 LST: (left) from experiment IDEAL and (right) from FAKEDRY. Orography is superimposed onto the figure in black contours with a 150-m interval. The CPRD is shown by the red box. Note the difference in color scales on the (left) and (right). The heavy black solid lines indicate the coastlines, and the heavy black dashed lines indicate the rainfall lines.

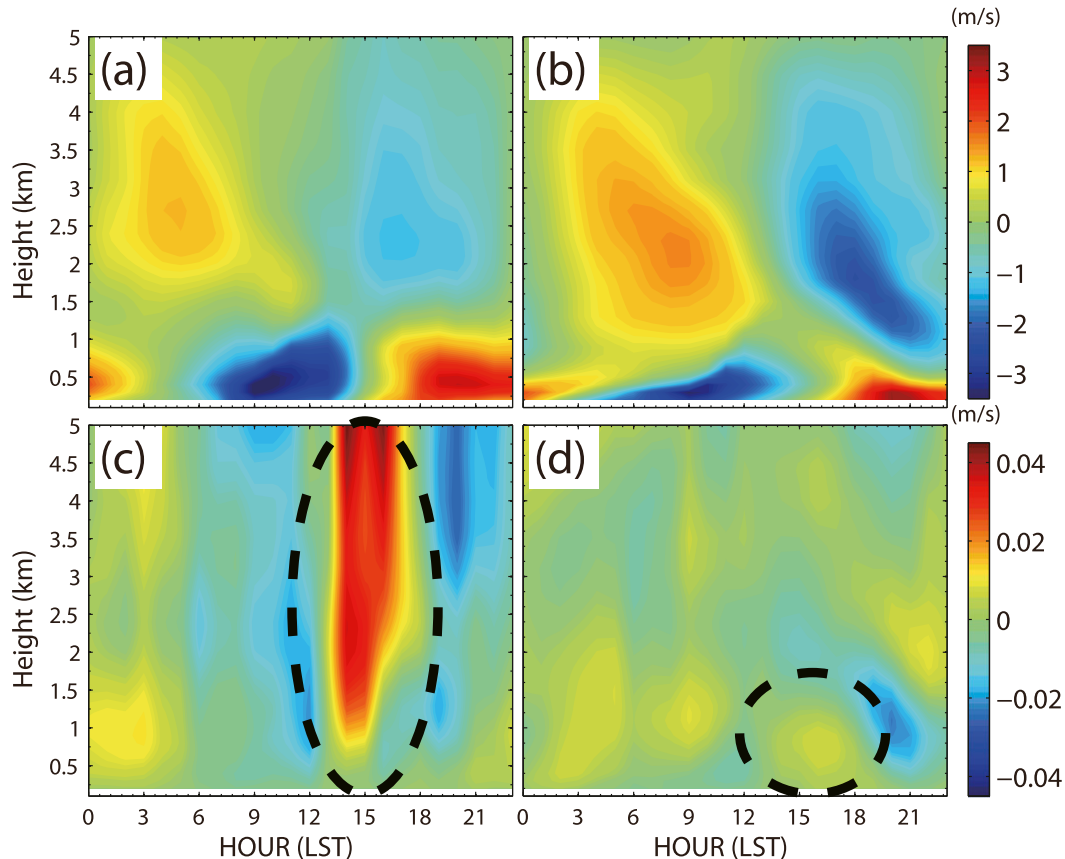


FIG. 13. Diurnal variations of vertical profiles over CPRD of v' and w' in (a),(c) IDEAL and (b),(d) FAKEDRY, respectively.

IDEAL. Inland propagation of the rainfall line in FAKEDRY is also slightly slower than in IDEAL, which reaches the center region of the Pearl River Delta (CPRD), as shown by the red box in Fig. 12, 1 h later than IDEAL.

The convective available potential energy (CAPE), convective inhibition (CIN), level of free convection (LFC), and lifting condensation level (LCL) over the CPRD in the IDEAL and FAKEDRY experiments have been calculated, respectively. Results show that the averaged atmospheric stabilities in the two experiments are similar over CPRD around the elapsed time of the sea breeze and the related rainfall line (from 1300 to 1600 LST). The CAPEs of IDEAL and FAKEDRY are 1467.7 and 1388.9 J kg^{-1} on average. In both experiments, CIN is too small (5.8 J kg^{-1} in IDEAL and 1.8 J kg^{-1} in FAKEDRY) to be of much significance. While the averaged LFCs (of IDEAL and FAKEDRY are 942.6 and 946.8 m) and LCLs (762.8 and 857.7 m) are similar in both experiments.

With similar atmospheric stabilities, the differences in rainfall intensities over the CPRD during afternoon may be induced by the dynamic and thermodynamic

differences between IDEAL and FAKEDRY. Diurnal variations of v' over the CPRD in IDEAL and FAKEDRY are shown in Figs. 13a and 13b. Negative (positive) v' represents the offshore (onshore) wind. The height of the land-and-sea-breeze top over the CPRD in IDEAL is around 1.2 km (Fig. 13a) and near 1.0 km in FAKEDRY (Fig. 13b). The arrival time of the sea-breeze front in IDEAL is 1 h earlier than that in FAKEDRY. The convergence zone between the sea breeze and residual land breeze over the CPRD is also stronger and deeper in IDEAL, while the return flow above the land and sea breeze is stronger in the FAKEDRY experiment. Figures 13c and 13d show the diurnal variations of perturbation vertical wind speed in the IDEAL and FAKEDRY experiments. In IDEAL, clear updraft can be found around the elapsed time of the sea breeze and the related rainfall line (from 1300 to 1600 LST, shown by the black dashed circle in Fig. 13c). The updraft is weak below the LFC but increases dramatically above it. In FAKEDRY, the updraft is much shallower near the elapsed time of the sea breeze and the related rainfall line. However, the height of updraft in FAKEDRY is still

higher than LCL and LFC, and weak rainfall can still be produced over the CPRD (Figs. 12g,h). These results show that differences in both the dynamic and thermodynamic processes are responsible for the rainfall differences between these two experiments.

6. Summary and discussion

Complimentary to the observational study of C15, this modeling study investigates the diurnal variations of the land and sea breeze and related precipitation over the south China coastal region during the mei-yu seasons. Using high-resolution WRF simulations, particular emphasis is given to the impact of coastal mountains, dynamic, and thermodynamic forces on the diurnal cycles of the land and sea breeze and the associated rainfall. The WRF idealized simulation verified well against 3-yr averaged ground-based radar, surface, and CMORPH observations, along with the realistic diurnal variation and propagation of rainfall associated with the land and sea breeze over south China.

It was found that the diurnal cycle of precipitation over the south China coastal region during the mei-yu season can be divided into the nocturnal and daytime stages. From night to morning, an offshore rainfall line is initiated parallel to the coastline around 0000 LST, which subsequently propagates to the open sea. This nocturnal offshore rainfall is induced by the convergence between the prevailing low-level southerly wind and the counterpropagating land breeze. Apparent inhomogeneity of rainfall intensity can be found along this rainfall line, with heavier rainfall occurring in the region with higher coastal orography. A sensitivity experiment in which the terrain height is halved (HALF) shows that mountain breeze produced by coastal terrains can merge with the land breeze, resulting in increased intensity of offshore convergence and heavier precipitation during the nighttime (Fig. 14). During the daytime, a new rainfall line begins to form on the shore side of the coastline at noon and propagates to the inland area thereafter. This propagation is closely related to the inland penetration of the sea breeze. Mountains near the coastline retard the inland penetration of the sea breeze for the first few hours of the starting sea-breeze circulation. A gust front produced by the rainfall line further induces a new rainfall line on the southern slope of the inland mountains during late afternoon.

The impact of cold pool and latent heating release on the evolution of the land and sea breeze and related rainfall diurnal variations are further examined through two additional sensitive experiments that are performed with a similar setup to the control experiment (IDEAL). In an experiment that only turned off latent cooling from the evaporation of liquid water (NOVAP), the

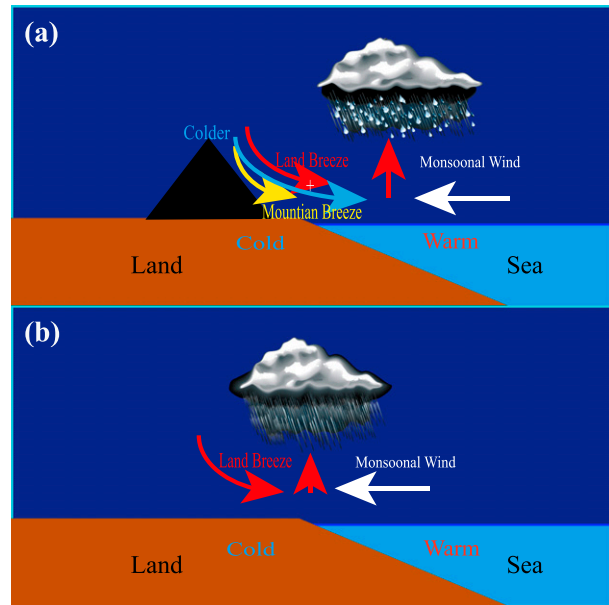


FIG. 14. Schematic diagrams of the nocturnal offshore rainfall in the regions (a) with and (b) without coastal orography.

inland-penetrating speed of the sea breeze and its related rainfall line becomes much slower than in IDEAL. Because the cold pool formation from moist convection is essentially shut off, no gust front can be found in front of the rainfall line associated with the sea breeze in NOVAP. In another experiment that turned off all latent heating and cooling (FAKEDRY), the inland-penetrating speed of sea breeze and its related rainfall line is slower than IDEAL but faster than NOVAP, indicating that the convection initiated by sea breeze can prevent the inland penetration of the sea breeze, while the cold pool produced by the convection can increase the inland-propagation speed of the sea breeze. Comparison of precipitation between IDEAL and FAKEDRY shows that the inland propagation of the rainfall line associated with the sea breeze is similar between IDEAL and FAKEDRY, while the rainfall line in IDEAL arrives in CPRD 1 h earlier than that in FAKEDRY. However, the precipitation intensity is much weaker in FAKEDRY. Simulation results show that the convective available potential energy, convective inhibition, lifting condensation level, and level of free convection over the CPRD in IDEAL are similar to those in FAKEDRY around the elapsed time of the sea-breeze-induced rainfall line. Convergence ahead of the sea-breeze front in both experiments is strong enough to induce precipitation, while latent heating can strengthen the intensities of updraft and precipitation substantially.

Since the initial and boundary conditions used in this study are the averages of the 135-day reanalysis data,

larger-scale synoptic flow variability, such as that induced by midlatitude fronts and tropical cyclones, is filtered out. The complex interactions between the land and sea breeze and other synoptic systems and the influences on rainfall diurnal variations over the region are the subjects of future investigation. For example, based on long-term radar observations, X. C. Chen et al. (2014) found that the strength of the low-level jet can dramatically change the pattern of rainfall spatial distribution over south China. Under the influence of a strong low-level jet, the rainfall will be heavier and more concentrated along the coastline over south China. Further modeling studies are also needed to provide deeper insight into the mechanisms of coastal precipitation under the influence of the low-level jet with varying intensity. The 4-km grid spacing used in this study may be insufficient in fully resolving weakly forced circulations like the horizontal convective rolls that can be important in the land- and sea-breeze precipitation process (Fovell 2005). Future investigations with higher spatial resolutions are planned to study the importance of weakly forced circulations on the land- and sea-breeze-related precipitation over south China. In addition, the vertical structure of precipitating clouds and variation of surface flux over the region also require further investigation, as was done in Saito et al. (2001) and Persson et al. (2005).

Acknowledgments. This work was primarily supported by the National Fundamental Research 973 Program of China (2013CB430101), the Social Common Wealth Research Program (GYHY201006007), the National Natural Science Foundation of China (Grants 41275031 and 41322032), the Program for New Century Excellent Talents in Universities of China, and was also partially sponsored by NSF Grants 0904635 and 1114849. The author Xingchao Chen thanks the Department of Meteorology at Penn State University for hosting his visit. Computing was performed at the Texas Advanced Computing Center (TACC).

REFERENCES

- Atkins, N. T., R. M. Wakimoto, and T. M. Weckwerth, 1995: Observations of the sea-breeze front during CaPE. Part II: Dual-Doppler and aircraft analysis. *Mon. Wea. Rev.*, **123**, 944–969, doi:10.1175/1520-0493(1995)123<0944:OOTSBF>2.0.CO;2.
- Baker, R. D., B. H. Lynn, A. Boone, W.-K. Tao, and J. Simpson, 2001: The influence of soil moisture, coastline curvature, and land-breeze circulations on sea-breeze-initiated precipitation. *J. Hydrometeor.*, **2**, 193–211, doi:10.1175/1525-7541(2001)002<0193:TIOSMC>2.0.CO;2.
- Banta, R. M., L. D. Olivier, and D. H. Levinson, 1993: Evolution of the Monterey Bay sea-breeze layer as observed by pulsed Doppler lidar. *J. Atmos. Sci.*, **50**, 3959–3982, doi:10.1175/1520-0469(1993)050<3959:EOTMBS>2.0.CO;2.
- Bao, X., and F. Zhang, 2013: Impacts of the mountain–plains solenoid and cold pool dynamics on the diurnal variation of warm-season precipitation over northern China. *Atmos. Chem. Phys.*, **13**, 6965–6982, doi:10.5194/acp-13-6965-2013.
- Barthlott, C., B. Adler, N. Kalthoff, J. Handwerker, M. Kohler, and A. Wieser, 2014: The role of Corsica in initiating nocturnal offshore convection. *Quart. J. Roy. Meteor. Soc.*, **142**, 222–237, doi:10.1002/qj.2415.
- Boybeyi, Z., and S. Raman, 1992: A three-dimensional numerical sensitivity study of convection over the Florida peninsula. *Bound.-Layer Meteor.*, **60**, 325–359, doi:10.1007/BF00155201.
- Bromwich, D. H., L. Bai, and G. G. Bjarnason, 2005: High-resolution regional climate simulations over Iceland using Polar MM5. *Mon. Wea. Rev.*, **133**, 3527–3547, doi:10.1175/MWR3049.1.
- Burpee, R. W., and L. N. Lahiffi, 1984: Area-average rainfall variations on sea-breeze days in south Florida. *Mon. Wea. Rev.*, **112**, 520–534, doi:10.1175/1520-0493(1984)112<0520:AARVOS>2.0.CO;2.
- Chen, G., 2009: Diurnal variation of precipitation over southeastern China: Spatial distribution and its seasonality. *J. Geophys. Res.*, **14**, D13103, doi:10.1029/2008JD011103.
- , W. Sha, and T. Iwasaki, 2009: Diurnal variation of precipitation over southeastern China: 2. Impact of the diurnal monsoon variability. *J. Geophys. Res.*, **114**, D21105, doi:10.1029/2009JD012181.
- , X. Zhu, W. Sha, T. Iwasaki, H. Seko, K. Saito, H. Iwai, and S. Ishii, 2015: Toward improved forecasts of sea-breeze horizontal convective rolls at super high resolutions. Part II: The impacts of land use and buildings. *Mon. Wea. Rev.*, **143**, 1873–1894, doi:10.1175/MWR-D-14-00230.1.
- Chen, T.-C., M.-C. Yen, J.-D. Tsay, C.-C. Liao, and E. S. Takle, 2014: Impact of afternoon thunderstorms on the land–sea breeze in the Taipei basin during summer: An experiment. *J. Appl. Meteor. Climatol.*, **53**, 1714–1738, doi:10.1175/JAMC-D-13-098.1.
- Chen, X. C., K. Zhao, and M. Xue, 2014: Spatial and temporal characteristics of warm season convection over Pearl River Delta region, China, based on 3 years of operational radar data. *J. Geophys. Res. Atmos.*, **119**, 12 447–12 465, doi:10.1002/2014JD021965.
- , —, —, B. W. Zhou, X. X. Huang, and W. X. Xu, 2015: Radar-observed diurnal cycle and propagation of convection over the Pearl River Delta during mei-yu season. *J. Geophys. Res. Atmos.*, **120**, 12 557–12 575, doi:10.1002/2015JD023872.
- Chien, F.-C., Y.-H. Kuo, and M.-J. Yang, 2002: Precipitation forecast of MM5 in the Taiwan area during the 1998 mei-yu season. *Wea. Forecasting*, **17**, 739–754, doi:10.1175/1520-0434(2002)017<0739:PFOMIT>2.0.CO;2.
- Crosman, E., and J. Horel, 2010: Sea and lake breezes: A review of numerical studies. *Bound.-Layer Meteor.*, **137**, 1–29, doi:10.1007/s10546-010-9517-9.
- Dai, A., F. Giorgi, and K. E. Trenberth, 1999: Observed and model-simulated diurnal cycles of precipitation over the contiguous United States. *J. Geophys. Res.*, **104**, 6377–6402, doi:10.1029/98JD02720.
- Dalu, G. A., and R. A. Pielke, 1989: An analytical study of the sea breeze. *J. Atmos. Sci.*, **46**, 1815–1825, doi:10.1175/1520-0469(1989)046<1815:AASOTS>2.0.CO;2.
- Drobinski, P., and T. Dubos, 2009: Linear breeze scaling: From large-scale land/sea breezes to mesoscale inland breezes. *Quart. J. Roy. Meteor. Soc.*, **135**, 1766–1775, doi:10.1002/qj.496.
- Dudhia, J., 1989: Numerical study of convection observed during the winter monsoon experiment using a mesoscale

- two-dimensional model. *J. Atmos. Sci.*, **46**, 3077–3107, doi:10.1175/1520-0469(1989)046<3077:NSOCOD>2.0.CO;2.
- Fovell, R. G., 2005: Convective initiation ahead of the sea-breeze front. *Mon. Wea. Rev.*, **133**, 264–278, doi:10.1175/MWR-2852.1.
- Freitas, E., C. Rozoff, W. Cotton, and P. S. Dias, 2007: Interactions of an urban heat island and sea-breeze circulations during winter over the metropolitan area of São Paulo, Brazil. *Bound.-Layer Meteor.*, **122**, 43–65, doi:10.1007/s10546-006-9091-3.
- Holland, G. J., J. L. McBride, R. K. Smith, D. Jasper, and T. D. Keenan, 1986: The BMCR Australian Monsoon Experiment: AMEX. *Bull. Amer. Meteor. Soc.*, **67**, 1466–1472, doi:10.1175/1520-0477(1986)067<1466:TBAMEA>2.0.CO;2.
- Hong, S.-Y., J. Dudhia, and S.-H. Chen, 2004: A revised approach to ice microphysical processes for the bulk parameterization of clouds and precipitation. *Mon. Wea. Rev.*, **132**, 103–120, doi:10.1175/1520-0493(2004)132<0103:ARATIM>2.0.CO;2.
- , Y. Noh, and J. Dudhia, 2006: A new vertical diffusion package with an explicit treatment of entrainment processes. *Mon. Wea. Rev.*, **134**, 2318–2341, doi:10.1175/MWR3199.1.
- Houze, R. A., S. G. Geotis, F. D. Marks, and A. K. West, 1981: Winter monsoon convection in the vicinity of north Borneo. Part I: Structure and time variation of the clouds and precipitation. *Mon. Wea. Rev.*, **109**, 1595–1614, doi:10.1175/1520-0493(1981)109<1595:WMCITV>2.0.CO;2.
- Joyce, R. J., J. E. Janowiak, P. A. Arkin, and P. Xie, 2004: CMORPH: A method that produces global precipitation estimates from passive microwave and infrared data at high spatial and temporal resolution. *J. Hydrometeorol.*, **5**, 487–503, doi:10.1175/1525-7541(2004)005<0487:CAMTPG>2.0.CO;2.
- Khain, A. P., I. Sednev, and V. Khvorostyanov, 1996: Simulation of coastal circulation in the eastern Mediterranean using a spectral microphysics cloud ensemble model. *J. Climate*, **9**, 3298–3316, doi:10.1175/1520-0442(1996)009<3298:SOCCIT>2.0.CO;2.
- Kingsmill, D. E., 1995: Convection initiation associated with a sea-breeze front, a gust front, and their collision. *Mon. Wea. Rev.*, **123**, 2913–2933, doi:10.1175/1520-0493(1995)123<2913:CIAWAS>2.0.CO;2.
- Kishtawal, C. M., and T. N. Krishnamurti, 2001: Diurnal variation of summer rainfall over Taiwan and its detection using TRMM observations. *J. Appl. Meteor.*, **40**, 331–344, doi:10.1175/1520-0450(2001)040<0331:DVOSRO>2.0.CO;2.
- Kousky, V. E., 1980: Diurnal rainfall variation in northeast Brazil. *Mon. Wea. Rev.*, **108**, 488–498, doi:10.1175/1520-0493(1980)108<0488:DRVINB>2.0.CO;2.
- Luo, Y., H. Wang, R. Zhang, W. Qian, and Z. Luo, 2013: Comparison of rainfall characteristics and convective properties of monsoon precipitation systems over South China and the Yangtze and Huai River basin. *J. Climate*, **26**, 110–132, doi:10.1175/JCLI-D-12-00100.1.
- Mapes, B. E., T. T. Warner, and M. Xu, 2003a: Diurnal patterns of rainfall in northwestern South America. Part III: Diurnal gravity waves and nocturnal convection offshore. *Mon. Wea. Rev.*, **131**, 830–844, doi:10.1175/1520-0493(2003)131<0830:DPORIN>2.0.CO;2.
- , —, —, and A. J. Negri, 2003b: Diurnal patterns of rainfall in northwestern South America. Part I: Observations and context. *Mon. Wea. Rev.*, **131**, 799–812, doi:10.1175/1520-0493(2003)131<0799:DPORIN>2.0.CO;2.
- Miller, S., B. Keim, R. Talbot, and H. Mao, 2003: Sea breeze: Structure, forecasting, and impacts. *Rev. Geophys.*, **41**, 1011, doi:10.1029/2003RG000124.
- Mlawer, E. J., S. J. Taubman, P. D. Brown, M. J. Iacono, and S. A. Clough, 1997: Radiative transfer for inhomogeneous atmospheres: RRTM, a validated correlated-k model for the longwave. *J. Geophys. Res.*, **102**, 16 663–16 682, doi:10.1029/97JD00237.
- Nicholls, M. E., R. A. Pielke, and W. R. Cotton, 1991: A two-dimensional numerical investigation of the interaction between sea breezes and deep convection over the Florida peninsula. *Mon. Wea. Rev.*, **119**, 298–323, doi:10.1175/1520-0493(1991)119<0298:ATDNIO>2.0.CO;2.
- Niino, H., 1987: The linear theory of land and sea breeze circulation. *J. Meteor. Soc. Japan*, **65**, 901–921.
- Persson, P. O. G., P. J. Neiman, B. Walter, J.-W. Bao, and F. M. Ralph, 2005: Contributions from California coastal-zone surface fluxes to heavy coastal precipitation: A CALJET case study during the strong El Niño of 1998. *Mon. Wea. Rev.*, **133**, 1175–1198, doi:10.1175/MWR2910.1.
- Qian, T., 2012: Topographic effects on the tropical land and sea breeze. *J. Atmos. Sci.*, **69**, 130–149, doi:10.1175/JAS-D-11-011.1.
- , C. C. Epifanio, and F. Zhang, 2009: Linear theory calculations for the sea breeze in a background wind: The equatorial case. *J. Atmos. Sci.*, **66**, 1749–1763, doi:10.1175/2008JAS2851.1.
- Rao, P. A., and H. E. Fuelberg, 2000: An investigation of convection behind the Cape Canaveral sea-breeze front. *Mon. Wea. Rev.*, **128**, 3437–3458, doi:10.1175/1520-0493(2000)128<3437:AIOCBT>2.0.CO;2.
- Rotunno, R., 1983: On the linear theory of the land and sea breeze. *J. Atmos. Sci.*, **40**, 1999–2009, doi:10.1175/1520-0469(1983)040<1999:OTLTOT>2.0.CO;2.
- Saito, K., T. Keenan, G. Holland, and K. Puri, 2001: Numerical simulation of the diurnal evolution of tropical island convection over the Maritime Continent. *Mon. Wea. Rev.*, **129**, 378–400, doi:10.1175/1520-0493(2001)129<0378:NSOTDE>2.0.CO;2.
- Segal, M., J. L. Song, R. A. Pielke, J. F. W. Purdom, and Y. Mahrer, 1986: Evaluation of cloud shading effects on the generation and modification of mesoscale circulations. *Mon. Wea. Rev.*, **114**, 1201–1212, doi:10.1175/1520-0493(1986)114<1201:EOCSEO>2.0.CO;2.
- Shen, Y., A. Xiong, Y. Wang, and P. Xie, 2010: Performance of high-resolution satellite precipitation products over China. *J. Geophys. Res.*, **115**, D02114, doi:10.1029/2009JD012097.
- Silva Dias, M., and A. J. Machado, 1997: The role of local circulations in summertime convective development and nocturnal fog in São Paulo, Brazil. *Bound.-Layer Meteorol.*, **82**, 135, doi:10.1023/A:1000241602661.
- Skamarock, W. C., and Coauthors, 2008: A description of the Advanced Research WRF version 3. NCAR Tech. Note NCAR/TN-475+STR, 113 pp., doi:10.5065/D68S4MVH.
- Steiner, M., R. A. Houze Jr., and S. E. Yuter, 1995: Climatological characterization of three-dimensional storm structure from operational radar and rain gauge data. *J. Appl. Meteorol.*, **34**, 1978–2007, doi:10.1175/1520-0450(1995)034<1978:CCOTDS>2.0.CO;2.
- Sun, J., and F. Zhang, 2012: Impacts of mountain–plains solenoid on diurnal variations of rainfalls along the mei-yu front over the east China plains. *Mon. Wea. Rev.*, **140**, 379–397, doi:10.1175/MWR-D-11-00041.1.
- Trier, S. B., C. A. Davis, and D. A. Ahijevych, 2010: Environmental controls on the simulated diurnal cycle of warm-season precipitation in the continental United States. *J. Atmos. Sci.*, **67**, 1066–1090, doi:10.1175/2009JAS3247.1.
- Walsh, J. E., 1974: Sea breeze theory and applications. *J. Atmos. Sci.*, **31**, 2012–2026, doi:10.1175/1520-0469(1974)031<2012:SBTAA>2.0.CO;2.
- Wang, C.-C., and D. J. Kirshbaum, 2015: Thermally forced convection over a mountainous tropical island. *J. Atmos. Sci.*, **72**, 2484–2506, doi:10.1175/JAS-D-14-0325.1.

- Wang, Y., J. Zhang, P.-L. Chang, C. Langston, B. Kaney, and L. Tang, 2016: Operational C-band dual-polarization radar QPE for the subtropical complex terrain of Taiwan. *Adv. Meteor.*, **2016**, 4294271, doi:[10.1155/2016/4294271](https://doi.org/10.1155/2016/4294271).
- Wapler, K., and T. Lane, 2012: A case of offshore convective initiation by interacting land breezes near Darwin, Australia. *Meteor. Atmos. Phys.*, **115**, 123–137, doi:[10.1007/s00703-011-0180-6](https://doi.org/10.1007/s00703-011-0180-6).
- Warner, T. T., B. E. Mapes, and M. Xu, 2003: Diurnal patterns of rainfall in northwestern South America. Part II: Model simulations. *Mon. Wea. Rev.*, **131**, 813–829, doi:[10.1175/1520-0493\(2003\)131<0813:DPORIN>2.0.CO;2](https://doi.org/10.1175/1520-0493(2003)131<0813:DPORIN>2.0.CO;2).
- Xu, W., E. J. Zipser, and C. Liu, 2009: Rainfall characteristics and convective properties of mei-yu precipitation systems over south China, Taiwan, and the South China Sea. Part I: TRMM observations. *Mon. Wea. Rev.*, **137**, 4261–4275, doi:[10.1175/2009MWR2982.1](https://doi.org/10.1175/2009MWR2982.1).
- Yang, M.-J., B. J. D. Jou, S.-C. Wang, J.-S. Hong, P.-L. Lin, J.-H. Teng, and H.-C. Lin, 2004: Ensemble prediction of rainfall during the 2000–2002 mei-yu seasons: Evaluation over the Taiwan area. *J. Geophys. Res.*, **109**, D18203, doi:[10.1029/2003JD004368](https://doi.org/10.1029/2003JD004368).
- Yu, C.-K., and B. J.-D. Jou, 2005: Radar observations of the diurnally forced offshore convective lines along the southeastern coast of Taiwan. *Mon. Wea. Rev.*, **133**, 1613–1636, doi:[10.1175/MWR2937.1](https://doi.org/10.1175/MWR2937.1).
- Yu, R., T. Zhou, A. Xiong, Y. Zhu, and J. Li, 2007: Diurnal variations of summer precipitation over contiguous China. *Geophys. Res. Lett.*, **34**, L01704, doi:[10.1029/2006GL028129](https://doi.org/10.1029/2006GL028129).
- Zhang, F., N. Bei, J. W. Nielsen-Gammon, G. Li, R. Zhang, A. Stuart, and A. Aksoy, 2007: Impacts of meteorological uncertainties on ozone pollution predictability estimated through meteorological and photochemical ensemble forecasts. *J. Geophys. Res.*, **112**, D04304, doi:[10.1029/2006JD007429](https://doi.org/10.1029/2006JD007429).
- Zhang, Y., Y.-L. Chen, T. A. Schroeder, and K. Kodama, 2005: Numerical simulations of sea-breeze circulations over north-west Hawaii. *Wea. Forecasting*, **20**, 827–846, doi:[10.1175/WAF859.1](https://doi.org/10.1175/WAF859.1).
- , J. Sun, and S. Fu, 2014: Impacts of diurnal variation of mountain-plain solenoid circulations on precipitation and vortices east of the Tibetan Plateau during the mei-yu season. *Adv. Atmos. Sci.*, **31**, 139–153, doi:[10.1007/s00376-013-2052-0](https://doi.org/10.1007/s00376-013-2052-0).